applied sciences

MDPI

Article

Assessing and Modelling the Interactions of Instrumented Particles with Bed Surface at Low Transport Conditions

Zaid Alhusban * and Manousos Valyrakis *

School of Engineering, University of Glasgow, Glasgow G12 8QQ, UK
* Correspondence: zaidhosban@gmail.com (Z.A.); Manousos.Valyrakis@glasgow.ac.uk (M.V.)

Featured Application: This research describes the application of an instrumented sphere for monitoring the vigorousness of its interactions as it is transported downstream a turbulent river. The presented tool has the potential to offer, in a novel and relatively accessible and direct way, information that links to the bed load transport rates in natural streams and built canals.

Abstract: Sediment transport at near threshold to low transport stages (below the continuous transport) can still be affected by flow turbulence and its dynamics can benefit from further comprehensive studies. This study uses an instrumented particle embedded with micro electromechanical sensors (MEMS) to allow tracking the motions and forces acting on it, leading to and during its transport. Instrumented particle transport experiments were carried out at laboratory flume under a range of flow conditions. The probability distributions functions (PDFs) of bed load particle instantaneous velocities, hop distances and associated travel times (measured from start to stop of transport) were obtained for all the performed experiments with varying flow rates and particle density. The modelled distributions are useful and enable a deeper understanding of bed load sediment transport dynamics from a Lagrangian perspective. Furthermore, the results analyzed from the instrumented particle (including the particle's transport mode) were validated using visual particle tracking methods (top and side cameras). The findings of this study demonstrate that for the range of turbulent flows trialed herein, the instrumented particle can be a useful, accessible, and low-cost tool for obtaining particle transport dynamics, having demonstrated satisfactory potential for field deployment in the near future.

Keywords: sediment transport; turbulent flows; particle hopping; probability distribution function (PDF); micro-electromechanical sensors (MEMS); river engineering

Citation: Alhusban, Z.; Valyrakis, M. Assessing and Modelling the Interactions of Instrumented Particles with Bed Surface at Low Transport Conditions. *Appl. Sci.* **2021**, *11*, 7306. https://doi.org/10.3390/app11167306

Academic Editor: Donatella Termini

Received: 15 May 2021
Accepted: 4 August 2021
Published: 9 August 2021

1. Introduction

1.1. Background to Bed Load Transport Processes

Sediment transport processes govern the stability of infrastructure near flowing water bodies as well as the ecology and geomorphology of many freshwater habitats, thus being important enough to have been studied for many decades [1,2]. Sediment transport is typically classified into bed load and suspended load, with the former commonly characterizing the transport of fine to coarse sediment traveling downstream with frequent contact with the bed. In contrast, suspended load refers to very fine sediment (practically comprising of finer particles such as silts, fine sands, and clays) transported above the bed load layer. Several processes in fluvial hydraulics such as erosion, deposition, scour, and the generation and disintegration of bed-forms are largely governed by bed load sediment transport [3–8].

Sediments initially resting on the bed surface may jump, slide, and roll downstream, when near-bed surface flow conditions exceed the threshold for particle entrainment. Therefore, corresponding modes of transport, namely rolling, sliding, and saltation, have been used to describe these distinct, highly dynamical processes and the reasons leading

to their occurrence, as well as rate of occurrence (see Figure 1 for a visual description of these processes). Whether a sediment particle is transported by one or another bed load transport mode is controlled by the combination of flow and sediment particle properties, greatly affecting their dynamical interactions. The mode of bed load transport has been found to depend on the ratio of the settling velocity and the shear velocity [9], while other research has shown the relevance of the particle Reynolds number as defining the saltation processes [10], also irrespective of particle size.

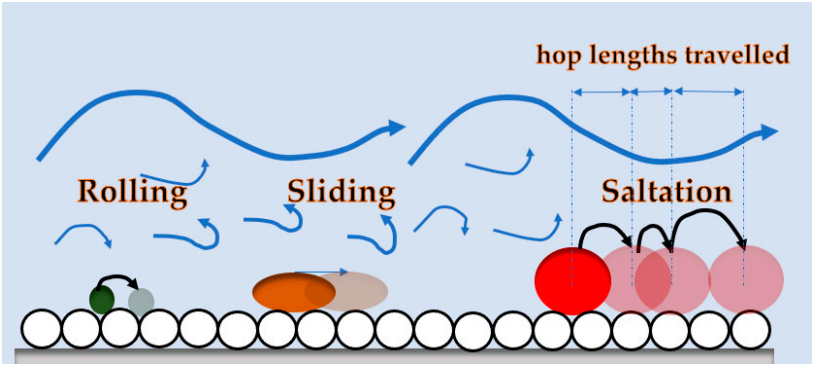

Figure 1. Schematic demonstrating the main modes of bed load transport by rolling, sliding, and saltation, shown in green, orange, and red colors, respectively. The initial resting position is shown with a dark colored particle, while the transported particle position is illustrated with the lighter respective colors. Note the variable hop distances traveled downstream by a saltating particle, as governed by highly dynamical complex three-way (particle-turbulent flow-bed surface) interactions.

For example, the rolling mode occurs when a relatively more rounded particle translates over the ridge formed by the tops of the sediment particles forming the bed surface. For flows very close and below the threshold of motion, only small but noticeable twitching or vibrating motions may be observed, for both aeolian [11] and fluvial [12,13] bedload transport. Near (and just above) threshold flow conditions are capable of intermittently displacing a particle resting on the bed surface over a short downstream distance (typically an order of the particle's diameter), depending on the frequency and magnitude of occurrence of sufficiently energetic flow events [14] (e.g., see green particle in Figure 1). The slide mode usually occurs for relatively platy particles, when the instantaneous drag forces overcome the resistance to friction at the contact points of particle and the bed surface, making it slip over the top of the bed surface. The elongated or platy shape of the sediment particle renders it difficult to rotate (and roll) around its axis, yet the particle's size and lack of sufficient pressure forces mean that it will effectively be transported while retaining contact with the bed surface throughout its motion [15].

Saltating motions are the dominant (in terms of the percentage of material transported or the portion of the mean transport time of individual particles being transported [3,16,17]) mode of transport for flows above the incipient motion threshold. Depending on the flow (including the magnitude of mean flow and turbulence intensity) and particle characteristics, saltating particles may move in small hops to larger ballistic-like motions, near the bed surface. This process is largely happening without maintaining continuous contact with the bed surface (as opposed with rolling or sliding modes of transport).

Transport in saltation mode typically occurs with a series of particle jumps, the characteristics of which (e.g., height and downstream length) are governed by sediment particle (including shape, density and size), bed surface (roughness, forms and slope), and flow (mean shear stresses, turbulence intensity or occurrence of energetic flow events) properties, leading to its downstream transport [14,18]. Consecutive particle jumps, typically termed as particle "hops", move between adjacent bed surface contacts, exchanging energy with the flow (offering energy for transport) and solid interface (and abruptly dissipating transport energy out due to collisions). These hops will naturally have a variable lengthscale

governed by the instantaneous interactions of the particle with its surrounding flow field, resulting in a range of hop distances per transport event (see saltation event shown in Figure 1). As a result, an above-threshold flow will have a distribution of hop distances characteristic of these interactions [19].

1.2. Conceptual Description of Transport Processes by Hopping

Laboratory experiments have not only been essential in developing empirical bed load equations, but they have also been used to clarify some of the more detailed processes and mechanics in sediment transport from near above-threshold to higher solids transport flow conditions [16–18]. As mentioned before, the dominant mode of bed load transport is saltation, characterized by particle hops or bounces along the bed surface. This is due to the action of hydrodynamic forces exceeding the resisting component of its submerged weight. A typical demonstration for particles laying in a bed surface of slope α, transported by saltation a range of particle packings and local arrangements and hinderance from surrounding particles, is given in Figure 2. Sediment motion is initially driven by almost impulsive turbulent flow events (I_i), making the particle ascend for a certain distance (from a fraction of its diameter to a lengthscale comparable to its diameter), and then descend towards the bed surface, under the action of gravity, eventually ceasing its motion after one or more collisions with the particles comprising the bed surface [12]. Sediment movement (number of hops and individual hop characteristics) is controlled by the particle's collisions with the bed surface and driven by the resultant force, which comprises the component of the submerged particle's weight (W_{sub}), and hydrodynamic drag (F_D) and lift (F_L) force components, orthogonal to the particle's local coordinate system centered at its center of mass [20,21]. The almost impulsive [22] kick offered by the turbulent flow event towards pushing a particle out of its pocket by saltation is the temporal integral of the total force acting on the particle, for the duration where the driving hydrodynamic (combination of drag and lift) forces exceed the resisting forces (component of the submerged particle's weight), as shown in Figure 2. For the case of a fully exposed particle, the hydrodynamic drag has a greater potential of resulting in an incipient entrainment (for a coarse particle, see green colored particle in Figure 2). The applied drag force, F_D, can be estimated by the classical quadratic local flow velocity parameterization or as a function of the pressure differential between the upstream and downstream face of the particle, $F_D = (\Delta P_h)$ Aparticle, where Aparticle is the particle area projected on a plane perpendicular to the streamwise flow direction and ΔP_h is the pressure difference between the particle's upstream and downstream face [23]. For the fully exposed particle arrangement, Aparticle is about 87% of the area of the particle's cross-section, because of limited partial blockage by the upstream base particles. For greater ranges of partial hinderance (e.g., orange colored particle), this percentage will reduce all the way to zero for the case of fully buried particles (red colored particle, Figure 2). For the latter case, the impulsively applied lift force (F_L) is the driving force to lift the particle above its pocket, whenever it exceeds the submerged component of its weight. Hydrodynamic lift can be estimated as the pressure difference between the bottom and the top of the particle (ΔP_v) because of the velocity gradient near the bed surface, as $F_L = (\Delta P_v - \rho g D \cos\alpha)$ Aparticle, in which Aparticle = $\pi D^2/4$ is the particle area projected on a plane along the bed surface, and $\rho g D$ is the difference in hydrostatic pressure between the top and bottom of the particle [24–27]. In the case of a partially buried particle, which is the common case for loosely packed sediment particles (e.g., shown in orange color, Figure 2), a combination of drag and lift forces may contribute to the particle's saltation.

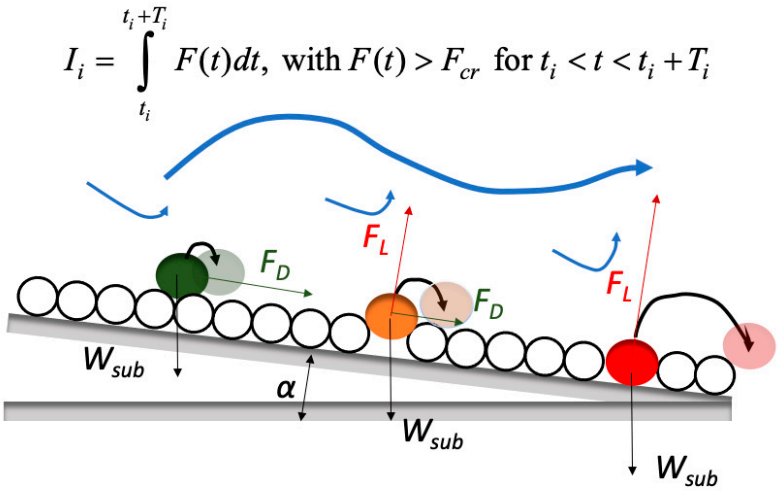

Figure 2. Demonstration of the dominant above-threshold hydrodynamic forcing modes for a particle hopping out of its pocket, leading to transport by saltation. Hydrodynamic impulse is defined as the temporal integral of the total force acting on the particle. This can primarily be the hydrodynamic drag (F_D), lift (F_L), or a combination of both forces, for the cases of a particle fully exposed, partially hidden, and buried in the bed surface (shown in green, orange, and red, respectively).

Transport of sediment particles by saltation has received extensive attention [28–31], being a significant subject in the field of the hydraulic and river engineering, as it relates to many hydraulic engineering challenges such as channel bed and bank destabilization [32], as well as central for the stability of hydraulic infrastructure against scour (such as bridge piers and abutments [33–36]). Understanding sediment hop dynamics can lead to insights into the formation of more coherent morphological structures on the bed surface, such as pebble clusters [37], ribs, and riffle pools [38].

Particle hop metrics are essential in describing bedload transport in saltation mode and can be used to understand the complexity of sediment dynamics, by using a range of derived variables such as hop length (Δx), hop travel time (Δt), and mean instantaneous particle velocities (V_{mean}). Hop length (Δx) is defined as the stream-wise distance travelled by one saltating particle, from the start of its motion to the end of its rebound. Hop travel time (Δt) is the time of particle transport elapsed between the start of its motion and the end of its rebound.

1.3. Lagrangian Observations of Transport Processes Facilitated via Novel Sensing Tools

Flow sensing and transport processes monitoring and instrumentation have gained increasing attention following the relatively recent technological advancements in the field of micro-electromechanical sensors (MEMS) that make it possible to record Lagrangian observations of individual sediment particles [39–45] and shed light on the dynamics of sediment transport processes at an extraordinary resolution and with high precision fused inertial measurement units, IMUs (e.g., via the use of robust and accurate accelerometers, gyroscopes, and magnetometers) [46–48]. Instrumented particles with a range of such sensors can be placed on the riverbed surface to simulate the response of light natural pebbles, exposed to a flow field that can set these into motion downstream a river. The main data logged are the components of particle accelerations in the particle's local coordinate system as well as angular displacements around these. As with all electronics, limitations of such devices revolve around the duration; they can be autonomously powered before a need to recharge or change a power source. This has not been an issue for controlled lab experiments, but it may become a constraint for long periods of field deployment, affecting the useful logging durations that can be achieved or requiring a compromise in terms of the number and frequency of data being logged. Novel miniaturized instrumented particles equipped with high precision accelerometer and gyroscope sensors have also

been developed, recording time series of acceleration and angular displacement, finding application for the monitoring of bed surface destabilization [47,49], and monitoring low mobility bedload transport conditions [48].

Given the highly dynamic and relatively intermittent character of saltating particles inherited by turbulent flows just above the threshold of incipient motion and the randomness of particle properties (such as size and shape) and local microtopography properties (bed surface particles' arrangement and packing), as well as the complex particle/particle and fluid/particle interactions during transport by hopping [37]. The statistical description of sediment transport by using probability distributions is useful due to extensive temporal and spatial irregularity of the factors which control it, such as local grain geometry, relative grain exposure, friction angle, and bed surface packing conditions [37,50]. Researchers [13,37,51–54] have studied sediment transport in a probabilistic context and attempted to relate it to the hydrodynamic properties of turbulent flows, while considering sediment transport at the particle scale. As a universally accepted criterion that robustly explains this dynamical process and stochasticity does not yet exist, the stochastic description of sediment transport dynamics at a high resolution using MEMS appears to be attractive [48].

1.4. Outlook for the Current Study

Herein, this research combines improved understanding of the saltating particle processes with advances in the MEMS sensing capabilities to deploy an instrumented particle monitors particle transport from a Lagrangian approach. This study focuses on assessing the potential of advanced sensing technologies (e.g., instrumented particle) to monitor individual sediment particle hop characteristics, through a series of controlled flume experiments, towards better understanding and quantifying the dynamical processes of sediment transport at the grain scale for above-threshold conditions. In this research, the results obtained from the analysis of sensor data are linked to sediment transport processes and validated using visual methods (particle tracking methods from video input from high-speed cameras, similar to [18], offering top and side views). In practice, the instrumented particle is used as a traditional stepper tracker (but for a sediment particle), and while offering novel dynamical metrics in unprecedented detail. The size and resolution of the sensor data sets presented in this work offer sufficient detail for robustly describing the probability distributions of hopping processes and derived metrics. It is found that the Lagrangian description of the instrumented particle hopping, using embedded IMU sensors, with detailed and high-resolution information, can offer refined statistics for the representation of dynamical sediment transport processes, as well as novel insights on the effect of changes of particle densities and turbulent flow rates and bed surface roughness on the characteristics of a particle's saltation.

2. Experimental Methodology

A set of well-controlled laboratory flume experiments have been designed and carried out using in-house developed instrumented particle devices (similar to [46–49]), to better understand what controls coarse sediment transport hopping dynamics downstream gravel-bed rivers. Below, the details of the experimental test section, equipment, and matrix are offered.

2.1. Experimental Set Up

The experiments for this study were conducted under a range of well-controlled, fully turbulent, and rough flow conditions to evaluate the performance of the instrumented particle at a 7 m useful length Armfield flume in the Water Engineering Lab at the University of Glasgow. The purpose of these experiments was to assess the transport rates and hopping characteristics of an instrumented particle of different solid densities, for a range of flow rates above entrainment threshold conditions (just above the threshold of motion and well below continuous transport). The flow rate through the test section was

controlled by adjusting the frequency of the pump using a controller for the pump inverter. The observations of this experiment were obtained from tests carried out using a flume with the following channel specifications: 10 m full length, up to 0.4 m deep, and 0.9 m wide. The flume walls comprise smooth transparent glass, which allows observing particle transport from the side.

The bed surface is hydraulically roughened using gravel and glass beads of similar size, in a well-packed arrangement (Figure 3). Specifically, the flat bed surface was roughened using two sets of well-packed glass beads, having a rectilinear (rhomboidal or tetrahedral) arrangement to render the bed surface relatively uniform and avoid complexities of bed formations affecting transport characteristics. Two bed surface roughnesses have been simulated using two distinct particle sizes to compose each (see bed surfaces A and B in Figure 3a,b, respectively). Bed surfaces A and B comprise unisize well-packed particles having nominal diameters of 1.5 cm and 3.15 cm, respectively, resulting in distinct macroscopic hydraulic roughness. The test section over which the instrumented particle is transported by saltation has dimensions of at least 150 cm and 50 cm in length and width (Figure 3), respectively, for each bed surface. At the downstream end of the flume, the test section is located at 1.75 m from the tailgate of the flume. Figure 4 shows photographs taken from video produced from the top cameras over each of the test sections, during actual experimental runs. The instrumented particle being transported over each bed surface roughness is also clearly shown (black sphere, with white marks to also help visually validate the rate of instrumented particle rotations).

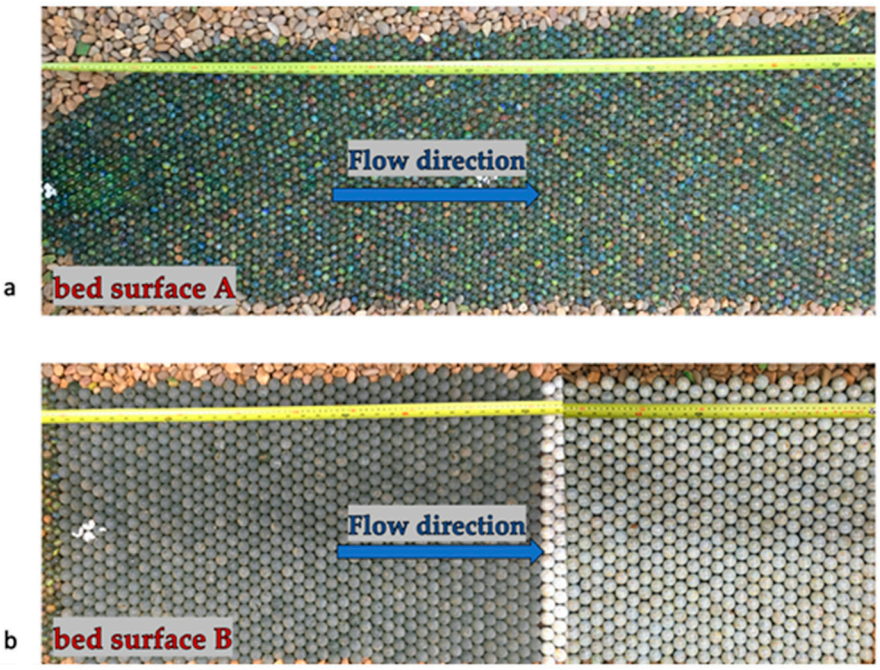

Figure 3. Illustration of the used bed surfaces: (**a**) A and (**b**) B, each comprising of well-packed tetrahedral arrangement of unisize marble beads of 1.5 and 3.15 cm, respectively, resulting in distinct bed surface roughness.

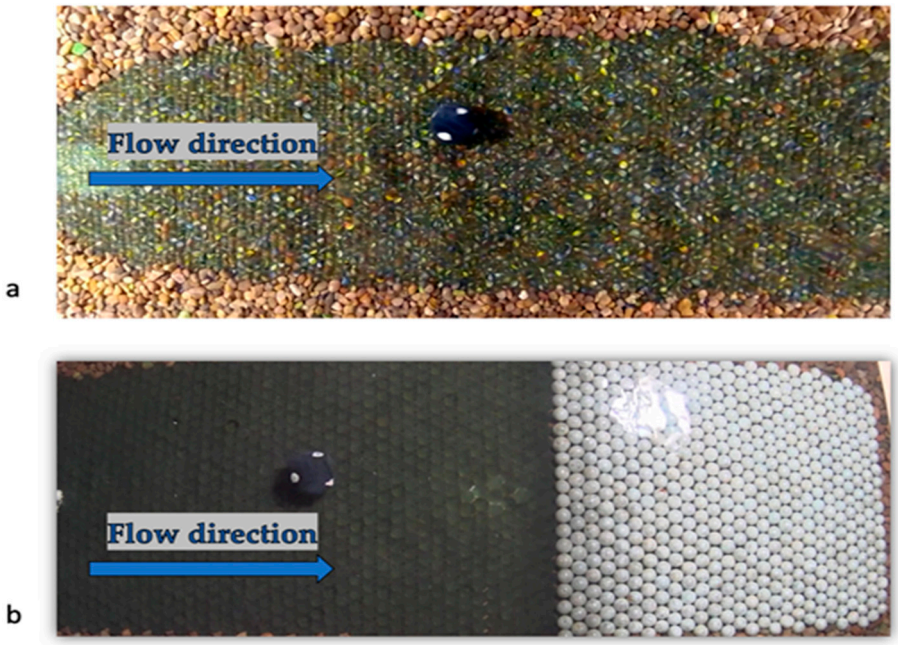

Figure 4. Photographs extracted from the videos obtained from the cameras placed atop the flume, illustrating the field of view captured during the experimental runs and covering the full extent of the experimental test section, for bed surface: (**a**) A and (**b**) B.

2.2. Experimental Equipment and Instrumentation

2.2.1. Flow Velocimetry

Instantaneous flow records were taken using a 3D Acoustic Doppler Velocimeter (Vectrino I © ADV, Nortek Inc., Providence, RI, USA), recording time series of local flow measurements at 25 Hz. Records of the local flow velocity along the water column were obtained to acquire mean flow velocity and turbulent intensity profiles. These allowed for the derivation of mean flow velocity and shear stress u_* (assuming logarithmic velocity profiles [54,55]) estimates for each of the flow rates trialed herein. Shields shear stresses τ_* are found using the bed shear stresses ($\tau_o = \rho u_*^2$), estimated from the shear velocity u_*:

$$\tau_* = \frac{\tau_o}{(\rho_s - \rho_w)gD} \quad (1)$$

where ρ_s and ρ_w are the densities of solid particle and water, respectively, g is the gravitational acceleration constant (g = 9.81 m/s^2), while the flow (Re) and particle (Re_*) Reynolds numbers are found using the particle's diameter (D) as a lengthscale and the mean flow U or shear velocity u_*, respectively:

$$Re = \frac{\rho U D}{\mu} \quad (2)$$

$$Re_* = \frac{\rho u_* D}{\mu} \quad (3)$$

Results of the above flow parameters are given in the sections below, including in a tabulated form in Appendix A. The flow rates are fully developed hydraulically rough, turbulent flows, referring to above-threshold flow conditions, for the range of solid particle densities used here.

2.2.2. Particle Transport Tracking: Visual Methods

The video input from high-speed cameras placed on the top and side of the flume allows for validation of the particle velocity estimated from the records taken from the IMU sensor fitted in the instrumented particle. The former visual technique offers a Eulerian-based description of the transport processes (i.e., [56]), where particle transport

rates are based on the particle's mean velocity estimated from direct video analysis. The test section was fully captured from the top cameras, as shown in Figure 4, showing example photographs of the particle in motion allowing to monitor sediment transport by saltation.

The video cameras were placed at a distance from the water surface to allow matching the field of view to the extent of the test section. Water surface light reflections were minimized by reducing ambient lighting and focusing strong light sources on the side of the flume (Figure 5). A high-speed commercial camcorder (GoPro Black Hero 7 © camera, Woodman Labs Inc., San Mateo, CA, USA) was used at high video resolution (HD) and 60 frames per second. The underwater side camera was fully submerged near the walls of the flume and far from the test section, positioned in a way to maximize the useful field of view as the particle is saltating downstream, and to avoid any direct flow interference (see Figure 5; field of view of the side camera is shown in the insert of Figure 5). From the top camera, video was recorded to cover the full length of the fake beds and to calculate the particle velocity in the upstream direction, while the rate of particle hopping, and modes of bedload transport were observed from the side camera. The rate of rotation of the instrumented particle can be also assessed by the side camera, as shown in the insert of Figure 5, which contains an illustration of the instrumented particle during its transport in saltation mode.

Figure 5. Demonstration of the experimental setup. (**a**) Top view of one of the beds roughnesses showing particle at rest. (**b**) Side view of one of the beds roughnesses showing the particle at motion phase.

2.2.3. Particle Transport Tracking: IMU Embedded Instrumented Particle

Specifically, the MEMS sensor embedded in a purpose-built 3D-printed shell offers an in-house designed instrumented device (similar to [46]) that is deployed herein (Figure 6) to study sediment transport processes with a comprehensive set of flume experiments. The MEMS sensors used are sensors logging data at a high frequency (200 Hz), encapsulated in a spherical shell. The casing of the instrumented particle involves a 3D-printed plastic shell with a diameter of 7.33 cm (Figure 6). The IMU sensor fitted in the instrumented particle yields a Lagrangian view of its transport by saltation, using sensor high resolution data. This can be an off-the-self IMU (e.g., 3-Space^{TM} Data Logger, Yost Labs Inc., Portsmouth, OH, USA) or a custom-made sensor (as designed and developed by [46]).

A magnetometer for orientation sensing relatively to the earth's gravitational field, a triaxial accelerometer for measuring particle accelerations (±16 g), and gyroscopes recording the rotations around the axis of the particle's local coordinate system (at a range of ±2000°/s) comprise the IMU. All these data can be fused (as shown in [48]) and are recorded at 200 Hz. A microcontroller is used to take data from the sensor and writes these to the external memory (microSD) from where the data can be downloaded to a personal computer for further analysis. The sensor benefits from accurate calibration routines, checking for the orthogonality of the axes of the sensor and a full 360° rotation test.

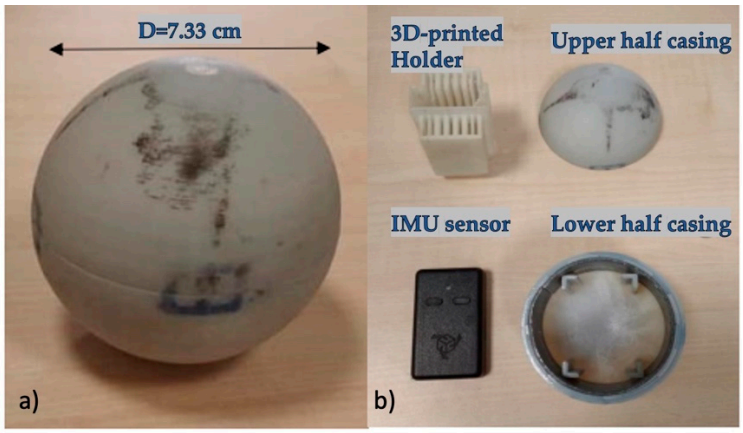

Figure 6. (**a**) The instrumented particle shell. (**b**) The instrumented particle with its internal components: inner casing, outer casing, sensor, O-ring, holder for sensor and density control.

Figure 6 shows the used instrumented particle with its internal components, including a 3D-printed holder, the IMU sensor, and the upper and lower half hemispheres. The lightweight casing of the sensor as well as the IMU size, along with the relative size of the casing (limited by the size of the IMU sensor), mean that the instrumented particle casing and sensor are having a solid density lighter than that of water (specific density <1). In order to achieve solid densities that will allow the instrumented particle to be transported as bedload in saltation mode, rectangular stripes of lead sheet shaped to fit the lower half casing (placed around the inner part of the lower half casing, like an O-ring, in Figure 6) and inside the 3D-printed holder, which also fits the IMU sensor. By fitting an appropriate number of stripes symmetrically (so as to balance the particle) within the holder (within the narrow gaps), specific instrumented particle densities can be achieved, in a repeatable fashion.

2.3. Experimental Matrix and Protocol

A range of parameters have been varied to assess and quantify their effect on the instrumented particle transport processes. Specifically, two distinct bed surface roughnesses have been used (surface A and B, Figure 3), four above-threshold flow rates have been tested for each bed surface, and four distinct solid densities have been used for the instrumented particle. The lower bound of the range of selected flow rates is found empirically by performing pilot experiments to assess the flow conditions that would just set the instrumented particle (with the higher solid density of instrumented particle) into motion. The highest flow condition was selected so that the transport duration downstream the test section for the fastest particle velocity (case with the lowest solid density of instrumented particle) would still suffice (offer enough data points) for the stochastic analysis of the obtained data. Ensuring that for all experimental runs, the shortest transport duration was above 10 s, allowed us to capture at least 2000 data points per experiment. For each of these 32 combinations, the instrumented particle was transported in saltation mode for a total of 5 repeats, resulting in a total of 160 experimental runs. This allows for assessing that the diversity of transport parameters is appropriately captured and stochastically well repre-

sented, as seen by the probabilistic analysis of the data (Section 3). For each of the above experiments, the appropriately weighted instrumented particles were manually placed at the top of the flume's bed surface along its centerline, at the start of an experimental run. The instrumented particle was fully exposed to the free stream flow and was released instantaneously to allow it being transported downstream.

3. Results

Instrumented particle accelerations and angular velocities for the range of flow and bed surface conditions were obtained by sensor data that were statistically analyzed to study the sediment transport dynamics. Instrumented particle velocities were also calculated from the videos of the transported particle obtained for validation of the sensor data. By using the time domain analysis of the sensor data (from a Lagrangian perspective), it is possible to quantify metrics of particle movements during their transport, such as hop lengths (Δx), hop travel time (Δt), mean particle velocity during transport (V_{mean}), and number of particle hops per second from a Lagrangian perspective from sensor data, whose reliable determination is not prevented by the size of the observation area as in the case of the visual method.

A particle's hop event can be identified from the sensor data as the difference between two adjacent maximum (representative of the start of the ascending phase after a rebound event with the bed surface) and minimum (representative of the instance of impact with the bed surface and loss of particle's mechanical energy) acceleration points. Thus, the hop travel time can be estimated from the time difference between the adjacent maximum and minimum acceleration points, while the hop length is the total distance travelled by a particle during the duration of the hop. One way of estimating travel distances is as the product of travel time with the mean particle velocity. The raw acceleration time series were extracted from the sensor for each experimental run. These were postprocessed (using a three-step window moving average) to remove signal errors. Then, a peak finding routine was used to identify consecutive peaks in the smoothed acceleration time series. Figure 7 shows a characteristic example of the particle's consecutive acceleration and deceleration phases for one of the runs (particle density 1180 kg/m^3).

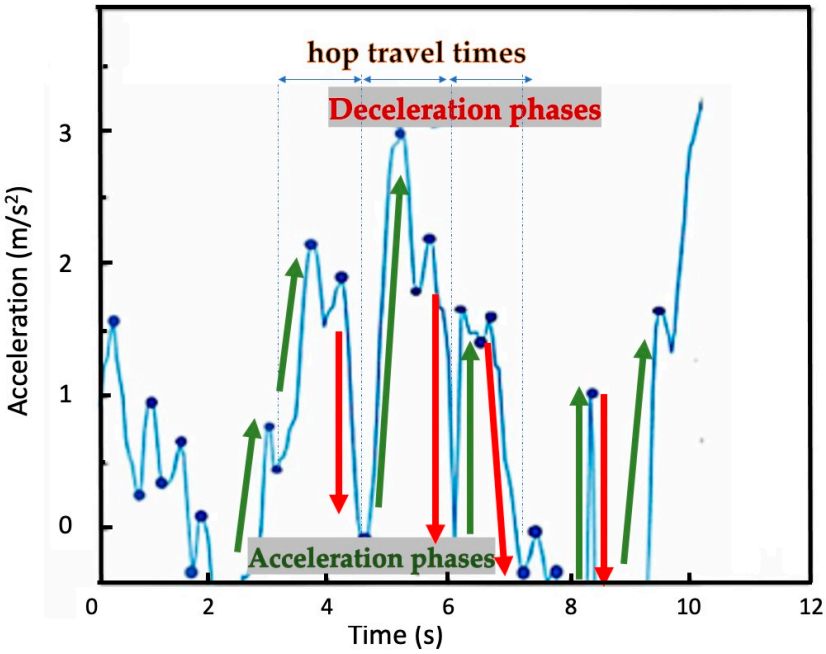

Figure 7. Acceleration time series for one of the trials showing consecutive accelerations (due to hydrodynamic forcing—see portions of the time series adjacent to the green arrows) and decelerating (due to collisions with the bed surface—see portions of the time series adjacent to the red arrows) phases.

The results for all of the instrumented particle transport experiments were checked from the top and side cameras to validate transport in saltation mode. As shown in Figure 7, the time between two adjacent maximum and minimum peaks gives the duration of particle acceleration (hop travel time). The hop length can be found as the total distance travelled during that duration. The mean particle velocity can be obtained by calculating the average of the particle's instantaneous velocity during transport. In the accelerating phase, particle velocity increases under the influence of hydrodynamic forces (function of the instantaneous flow velocity), which will show as an increasing acceleration (e.g., see segments of the time series next to the green arrows in Figure 7). The acceleration will cease suddenly when the particle hits one or more immobile bed surface particles and there will be a loss of some of the particle's mechanical energy. This impact with the bed surface will be seen as a sudden deceleration, which is observed as a negative peak in the time series of particle's acceleration (e.g., see segments of the time series next to the red arrows in Figure 7). The total number of hop events and their durations, throughout a particle's transport, can be found for each experimental run.

To assess how the instrumented particle's saltation processes are changing for different flow rates and particle densities, several metrics are estimated, including particle hop lengths, particle hop travel durations, mean particle velocity, and the frequency of particle hops (number of particle hops per second). The analysis of experimental results focuses on the statistical distributions of instrumented particle velocities, hop distances, and travel times, derived from sensor data. Stochastic predictive models of particle dynamics are described with these metrics along with their trends for a range of the flow conditions and instrumented particle and bed surface properties.

3.1. Hop Length

After Einstein's seminal work [51], sediment particle's hop distances have received a good amount of attention from several researchers such as [28–31], as it could be used to quantify bedload transport rates, if the rate of transport was considered [17,57]. The instrumented particle is transported with continuous hops throughout its advection downstream the test section and hop lengths were calculated from sensor data as the stream-wise distance travelled by one particle from the start of its motion to the end of its rebound. Numerous distribution fittings were assessed to obtain the best fit stochastic distributions for the different experimental runs, including Weibull, Beta, Gamma, normal, and exponential (Table 1). The Chi Square metric, describing how well each distribution fits the set of experimental observations by determining whether a significant difference between the observed values and measured values is expected under the model, was used to determine the best distribution fitting. The goodness of fit metric was used as follows:

$$X^2 = \sum \frac{(Oi - Ei)^2}{Ei} \quad (4)$$

where X = goodness of the fit, O_i = observed value, and E_i = expected value. Table 1 shows the goodness of fit results for different distributions of particle hop lengths for the minimum and maximum flow rates used in the range of experiments.

Table 1. Goodness of fit results and corresponding ranking for a range of distributions modelling hop travel distances for the minimum and maximum flow rates used in the experiment.

Model Distribution for Travel Distances	Goodness of Fit (for Q = 56 L/s)	Goodness of Fit (for Q = 42 L/s)	Rank
Weibull	1.28	1.64	2
Beta	3.54	1.92	3
Gamma	0.34	0.58	1
Normal	3.7	5.2	4
Exponential	6.4	7.1	5

Considering the goodness of fit metrics, Gamma was found to be the optimal distribution for modeling particle hop distances. Hop length was fitted by the Gamma probability distribution function model, as follows:

$$f_x(x) = \frac{1}{\Gamma(ax+1)\beta_x^{\alpha x+1}} x^{\alpha x} e^{\frac{-x}{\beta x}} \quad (5)$$

where x is the hop distance, αx and βx are the shape and rate (inverse scale) parameters, respectively, with $\alpha x > -1$ and $\beta x > 0$, and Γ is the gamma function. Figure 8 shows the probability density function (PDF) of measured hop lengths for the lowest flow rate of 49 (L/s), particle density of 1180 (kg/m^3), bed surface A, where the x-axis is the hop lengths (m), the y-axis is the count of hop events, and the red curve represents the Gamma distribution fit to the experimentally observed data.

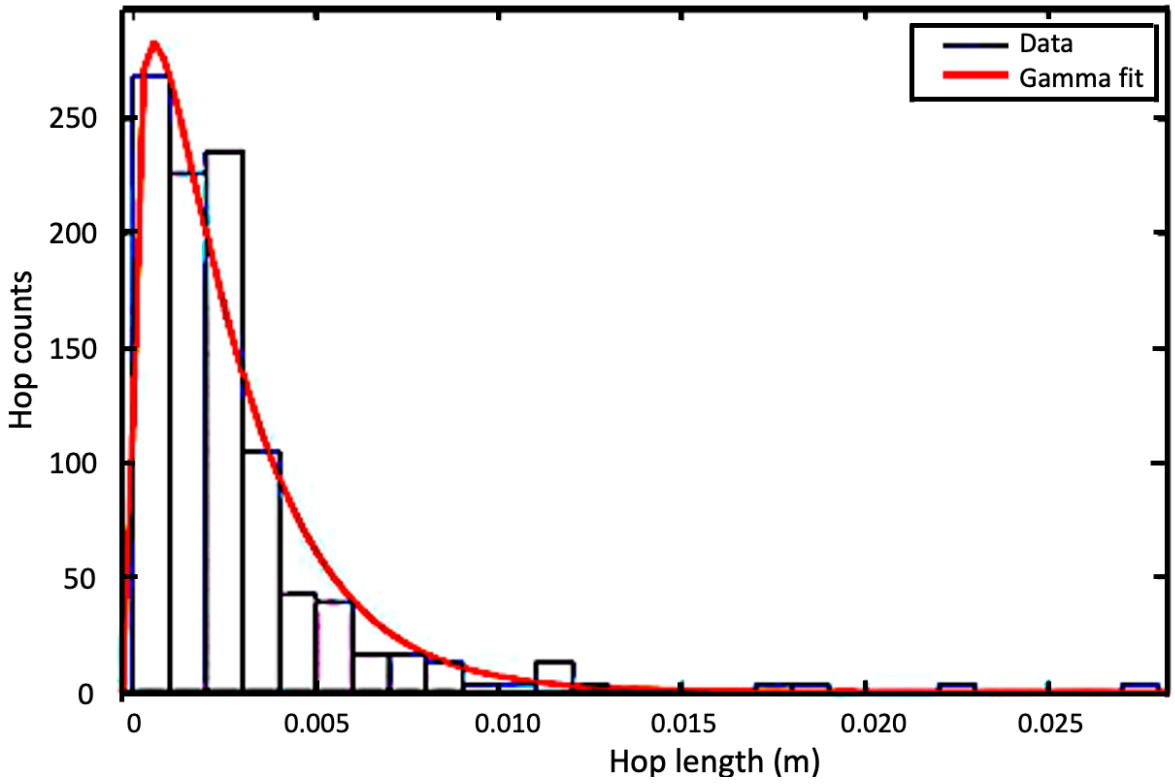

Figure 8. Empirical hop length data (m) and the best fit Gamma probability density function for the flow rate of 49 (L/s), instrumented particle density of 1180 (kg/m^3), and bed surface A.

As shown in Figure 8, the hop lengths were not hugely varied, and the Gamma function was the best fit for the measured hop lengths distributions, a similar finding

to [58], which also suggests the same distribution. In addition, it is similar to past research that has found exponential or Gamma (hop distance) distributions [57–62]. On the other hand, some researchers found different results, such as [29,30], who reported best fit for the Weibull distribution, as well as [63], who proposed the exponential distribution. The difference in the fitting distributions could be attributed to different control parameter settings used in this experimental study in comparison to the previous studies, as the used particle in this study is lighter, bigger in size, has higher flow Reynolds number ranges, and bed surface particles smaller to the saltating.

The research herein is the first to use an instrumented particle to assess hop distances, compared to previous studies that are based on high-speed imaging for a range of controlled flow conditions. In addition, the resolution of sensor data logging is quite high, set at 200 Hz, meaning that the instrumented particle is measuring every 5 ms, which allows capturing very short hop distances, over the range of flow conditions assessed herein.

3.2. Hop Travel Time

Hop travel times were calculated from sensor data as the time interval of particle movement from the start of its motion till the end of its rebound from the bed surface. Various distribution models, such as Weibull, Beta, Gamma, normal, and exponential, were applied to obtain the best fit for different hop travel times by using goodness of fit metrics.

Hop travel time (t) was fitted by an exponential function, as shown in the following:

$$f_t(t) = \frac{1}{t} e^{-\frac{t}{\bar{t}}} \quad (6)$$

where $\bar{t}$ is the mean hop travel time. Table 2 shows the hop travel time goodness of fit results for different distributions, for the minimum and maximum flow rates used in experimental runs. By using goodness of fit metrics (such as Chi square), the exponential was found to be the optimal fitting distribution for modeling the hop travel times, for both assessed bed surfaces.

Table 2. Goodness of fit results and corresponding ranking for a range of distributions modelling hop travel times for the minimum and maximum flow rates used in the experiment.

Model Distribution for Travel Times	Goodness of Fit (for Q = 56 L/s)	Goodness of Fit (for Q = 42 L/s)	Rank
Weibull	4.1	4.6	4
Beta	3.2	2.8	3
Gamma	6.4	7.1	5
Normal	1.4	1.8	2
Exponential	0.4	0.6	1

Figure 9 shows the empirical hop time intervals data and best fit probability density function (PDF) for the flow rate of 52.5 (L/s), particle density 1180 (kg/m^3), surface B, where the *x*-axis is the hop travel time (in seconds), the y-axis is the event counts, and the red curve represents the exponential distribution best fitting the data.

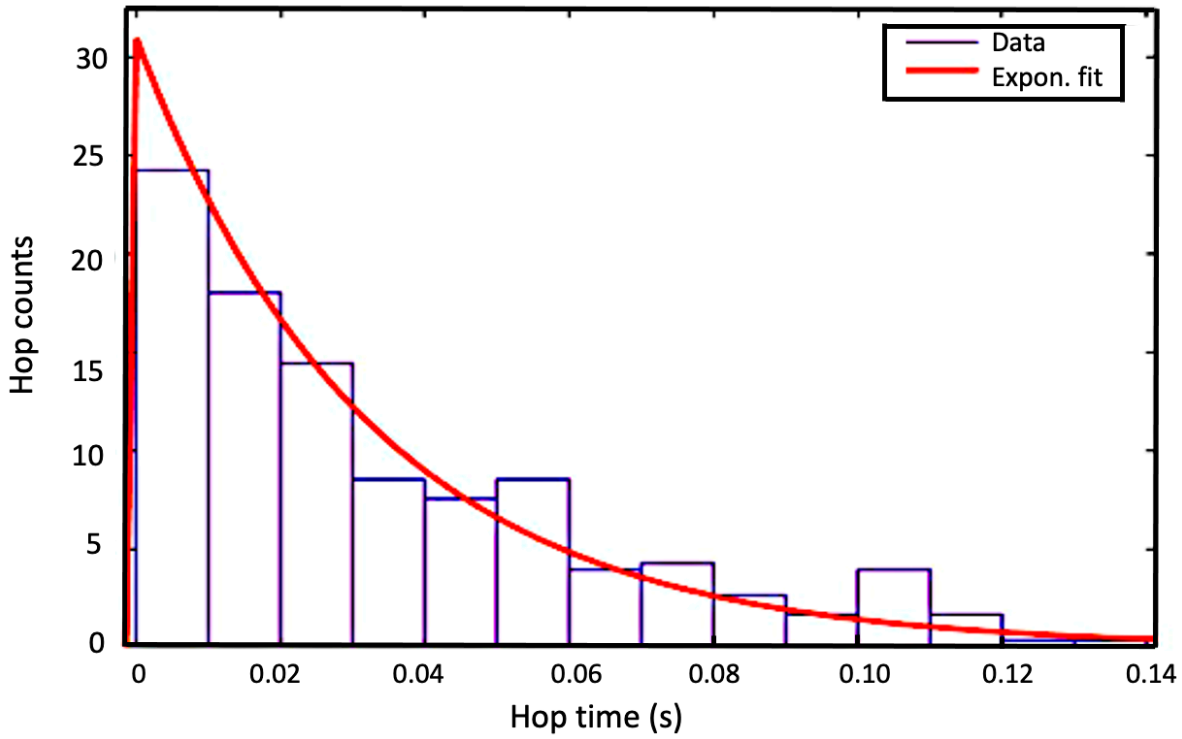

Figure 9. Distribution of empirical hop travel time data and corresponding best fit model (exponential probability density function) for the flow rate of 52.5 (L/s), particle density of 1180 (kg/m^3), and bed surface B.

As shown in Figure 9, the exponential function was the best fitting for the measured hop travel times distributions, which is the same best fit PDF found by [29,30,63,64].

3.3. Particle Velocity

A range of models have been trialed to obtain the best distribution fittings for the streamwise instantaneous particle velocities including Beta, exponential, Gamma, normal, and Weibull. Table 3 shows the mean particle velocity goodness of fit results for different distributions, for the minimum and maximum flow rates used in the experiment.

Table 3. Particle velocity goodness of fit results for minimum and maximum flow rates used in the experiment.

Model Distribution for Particle Velocities	Goodness of Fit (for Q = 56 L/s)	Goodness of Fit (for Q = 42 L/s)	Rank
Weibull	4.4	4.7	4
Beta	2.9	3.1	3
Gamma	5.6	6.2	5
Normal	1.7	2.1	2
Exponential	0.6	0.7	1

Using the goodness of fit metrics, the exponential distribution is found to offer the best fit to the particle velocities data. Instantaneous streamwise particle velocity (v) was fitted by the exponential function, as follows:

$$f_v(v) = \frac{1}{V_{mean}} e^{\frac{V_{mean}}{v}}, \; v >= 0 \tag{7}$$

where V_{mean} is the average particle velocity.

Figure 10 shows the instantaneous particle streamwise velocities modeled probability density function (PDF) for the flow rate of 49 (L/s), particle density of 1132 (kg/m^3) and bed surface A, where the x-axis is the magnitude of instantaneous particle velocities, the y-axis shows the event counts, and the red line represents the exponential distribution best fitting the experimentally observed data.

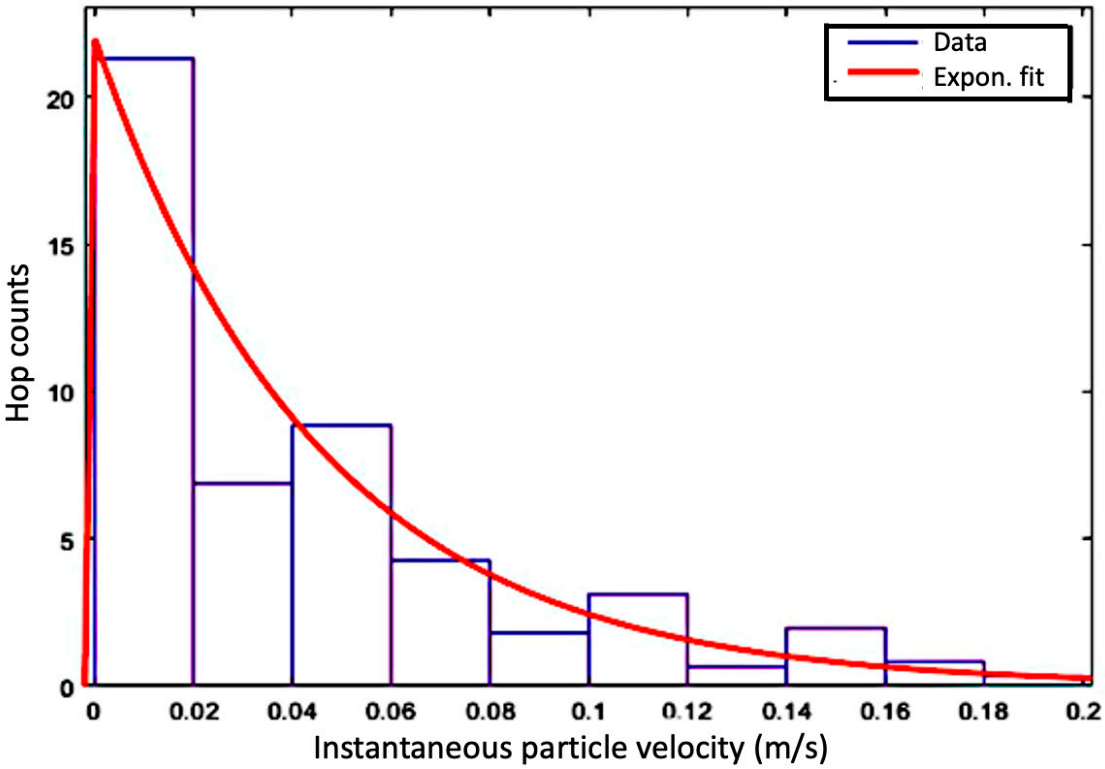

Figure 10. Empirical and modeled (exponential) distribution of instantaneous instrumented particle streamwise velocities for the flow rate of 49 (L/s), particle density of 1132 (kg/m^3), and bed surface A.

As shown in Figure 10, the exponential function was the best fitting of measured streamwise particle velocities distributions. The findings are consistent with those reported by [30,31,58], which also identified the exponential probability distribution models for the streamwise instantaneous velocities as the best fitting. In contrast, other studies [64–67] found that the Gaussian distribution offered the closest match to the empirical data of streamwise particle velocities. The differences in these findings are probably best attributed to the different range of particle mobility assessed in these studies: herein, the lowest particle mobility conditions are found to be best fit by exponential particle velocity models, while for flow conditions near the continuous or bulk bedload transport rates, the normal model may yield a better predictive value.

4. Discussion

4.1. Dependence of Hop Travel Distance on Particle and Flow Features

The research herein is the first to use an instrumented particle to assess hop distances. Particle hop lengths can be obtained from the Gamma distribution fittings of different particle densities and channel flow rates to assess and quantify any interesting trends. Greater magnitudes of hop lengths imply that the particle will transverse a distance along the channel with a smaller number of interactions with the bed surface. Figure 9 shows the comparison of the modelled hop lengths distributions (using the Gamma PDF) for the range of assessed particle densities and flows (defined with flow Reynolds number).

From Figure 11a,c, the extent and extrema of particle hop length distributions are seen to increase with increasing flow Reynolds number for both surfaces (A and B). For example,

as seen in Figure 11c (also Table 4, offered in Appendix A), for the bed surface B, the instrumented particle with density of 1132 kg/m^3 will travel a maximum hop distance 160% greater (from 0.0009 to 0.00235 m), for a 15% increase in flow Reynolds number (from 41,841 to 47,379). In addition, a similar trend is observed as the particle density decreases (Figure 11b,d), with the range of hop lengths increasing with solid particle densities, for both surfaces. For example, as seen in Figure 11b (bed surface A and Reynolds number of 50,789—also Table 5, offered in Appendix A), when particle density decreased by 10% from 1180 to 1085, the peak hop length increased about 70% (from 0.0019 to 0.0032 m). The effects of different particle densities and flow Reynolds number on the Gamma distribution parameters modelling hop lengths are also tabulated in Tables 4 and 5, offered in Appendix A, along with further discussion, to allow for a clearer representation of the variations in the body and specifically the tail of the distribution (that may be hard to discern in Figure 11).

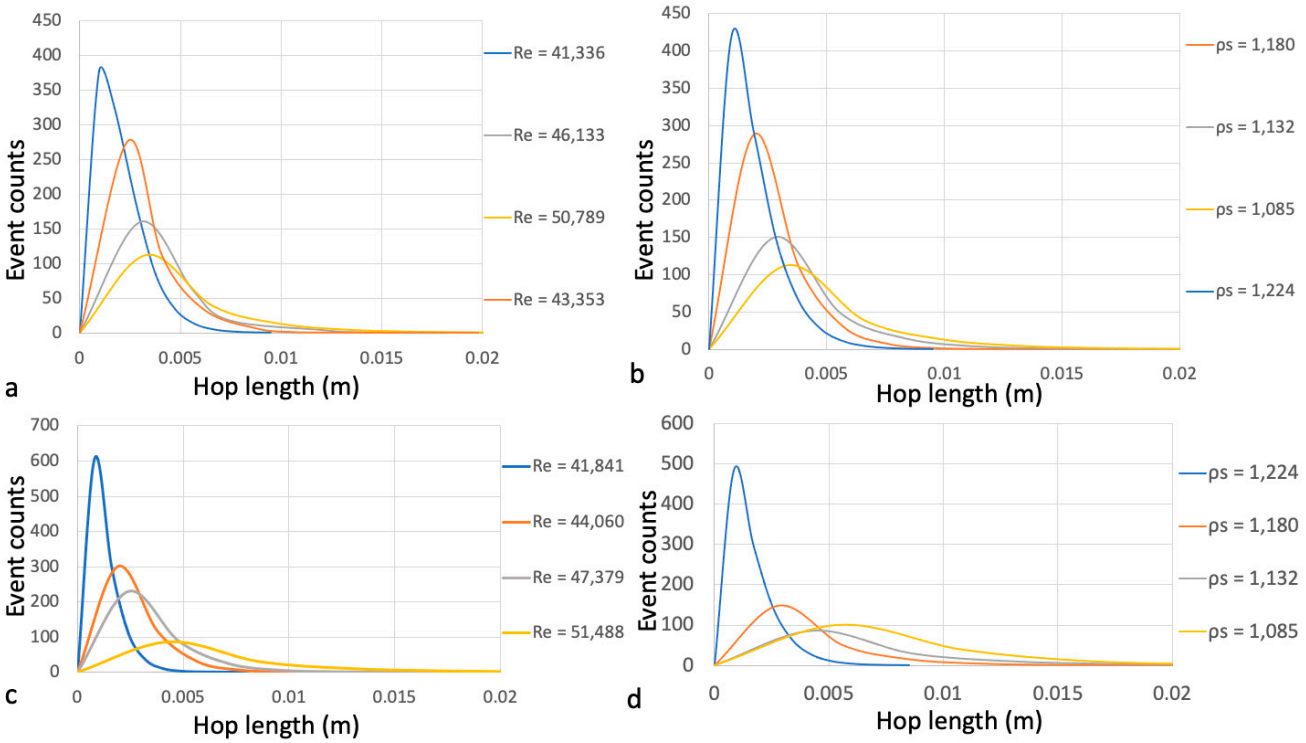

Figure 11. Hop length modelled by the Gamma distribution: (**a**) for different flow Reynolds numbers, bed surface A, and fixed instrumented particle density of 1132 kg/m^3, (**b**) for different instrumented particle densities, bed surface A, and fixed Reynolds number of 50,789, (**c**) for different flow Reynolds numbers, bed surface B, and fixed instrumented particle density of 1132 kg/m^3, and (**d**) for different instrumented particle densities, bed surface B, and fixed Reynolds number of 51,488.

Figure 12 shows the effect of flow Reynolds numbers and Shields numbers on its average hop length (modelled from the Gamma distributions fittings), for bed surfaces A and B, and the assessed particle densities.

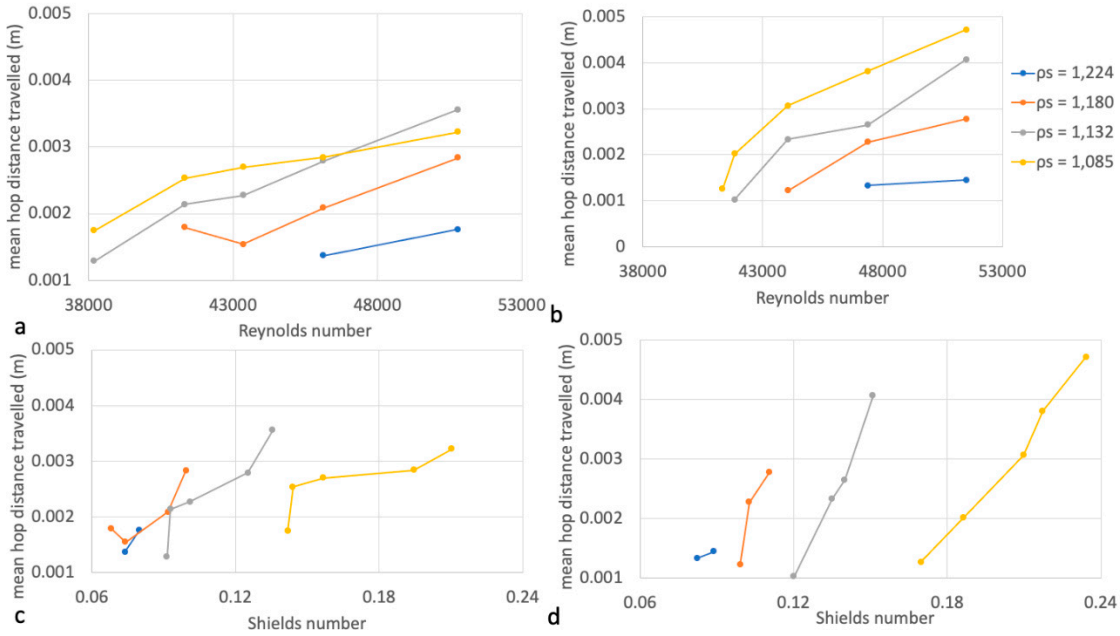

Figure 12. Mean hop distance travelled, for different instrumented particle densities: (**a**) against Reynolds number, for bed surface A, (**b**) against Reynolds number, for bed surface B, (**c**) against Reynolds number, for bed surface A, and (**d**) against Reynolds number, for bed surface B.

Figure 12 displays that the average hop length in general increases with lower particle density. For the example of bed surface A, with fixed flow Reynolds number of 50,789 (Figure 12c), the average hop length increases by 80% from 0.018 to 0.032 m, when particle density decreases by about 15% (from 1224 to 1085 kg/m^3). The average hop length increases with higher flow Reynolds (Figure 12a,b) and Shields (Figure 12c,d) numbers. For the example shown in Figure 12a, mean hop travel distance increases from 0.015 to 0.028 m (90%) with only about 15% increase in flow Reynolds number (from 43,353 to 50,789). The same increase is seen in Figure 12c, for increasing the Shields number from 0.074 to 0.099 (35%), for fixed particle density of 1180 kg/m^3 and bed surface A. With a higher Shields number and lower density, there is a higher hopping (saltation) length on average, as the particle interacts with the bed fewer times, while covering the same distance downstream. These results are significant as they demonstrate that for this still relatively low transport regime (above threshold), relatively slight increases in flow rates cause big increases in mean hop lengths.

For bed surface B, when the flow Reynolds number increases by 25% (from 41,337 to 51,488), the average hop length increases about fourfold (from 0.013 to 0.067 m) for fixed particle density of 1085 kg/m^3 (Figure 12b). Likewise, for a particle density decrease of about 15% from 1224 to 1085 kg/m^3, the average hop length increases from 0.015 to 0.067 m (350%), which shows how the lighter particle density multiples mean hop lengths for fixed flow Reynolds number of 51,488 (Figure 12b). With a higher Shields number, the particle has a higher hop length. For the example shown in Figure 12c (with fixed flow Reynolds number of 44,060), for a Shields number that doubles from 0.099 to 0.210, the particle's mean hop length increases by 150% (from 0.012 to 0.03 m).

In conclusion, hop lengths increases primarily with higher flow velocity, and are inversely dependent on particle's specific density, similar to the trends found by [58,60]. When there is increase in tractive bed shear stresses (e.g., Shields number), the total distance travelled will increase. Figure 12a,b, illustrates that with increasing channel flow Reynolds number or decreasing particle density, the particle interacts with the bed surface in fewer instances, and will therefore achieve greater hop lengths. As a result, the sensor data validate the expected outcomes. The bed surface with greater particle roughness size (bed

surface B) offers macroscopically a greater resistance to bedload transport, resulting in greater transport times for the two cases of lighter particles.

4.2. Dependence of Hop Travel Time on Particle and Flow Features

The mean hop travel times for particle motion can be obtained from exponential distribution fittings. Here, these are compared for different particle densities, flow Reynolds numbers, and bed surfaces. The mean particle hop travel times can be considered as an important characteristic for particle transport, as it gives an indication about the particle instantaneous velocities, as well as changes in the number of particles hop events. For high particle travel times, the same transport distances are transversed over a longer period and particles' instantaneous velocities are lower. Figure 13 shows comparisons of exponential distribution fittings for measured particle travel times, for different particle densities and the flow Reynolds numbers assessed herein.

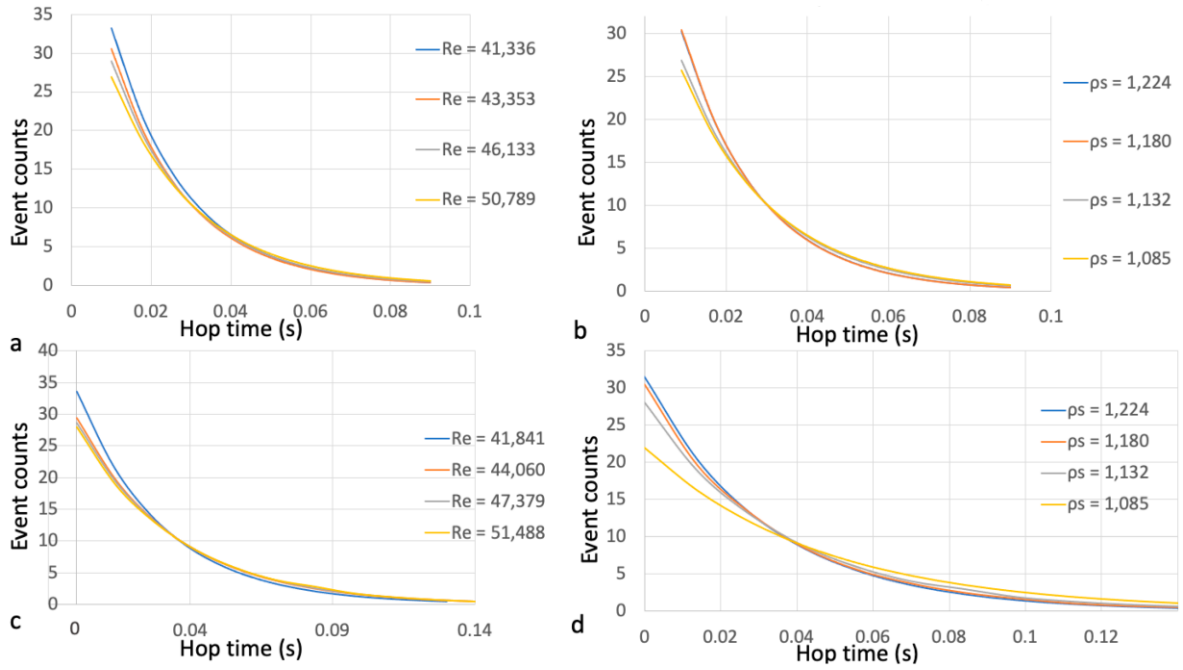

Figure 13. Hop time modelled by the exponential distribution: (**a**) for different flow Reynolds numbers, bed surface A, and fixed instrumented particle density of 1132 kg/m^3, (**b**) for different instrumented particle densities, bed surface A, and fixed Reynolds number of 50,789, (**c**) for different flow Reynolds numbers, bed surface B, and fixed instrumented particle density of 1132 kg/m^3, and (**d**) for different instrumented particle densities, bed surface B, and fixed Reynolds number of 51,488.

From Figure 13a,c, it is seen that with increasing flow Reynolds number, the probability of occurrence of higher particle travel times increases for both bed surfaces, and even more for the rougher bed surface (B). For example, in bed surface A (Figure 13a), when flow Reynolds number increased by about 15% (from 43,353 to 50,789), the probability of occurrence increased by 45% (from 0.426 to 0.624) for the same particle hop travel time of 0.09 s. In addition, the probability of occurrence of higher particle hop travel times increases for both bed surfaces as the particle density decreases (Figure 13b,d). For example, for bed surface B, when particle density decreased by about 15% (from 1224 to 1085 kg/m^3), the probability of occurrence increased from 0.38 to 1.01 (165%) for the same particle hop travel time of 0.14 s. The effects of different particle densities and flow Reynolds number on the fitted exponential distribution parameters modelling hop travel times are also tabulated in Tables 6 and 7 in Appendix A, along with further discussion to allow for a clearer representation of the variations in the body and specifically the tail of the distribution (that may be hard to discern in Figure 13). Figure 14 shows the effect of different flow Reynolds

and Shields numbers and test particle densities on the average hop travel time modeled with the fit exponential distributions for bed surfaces A and B.

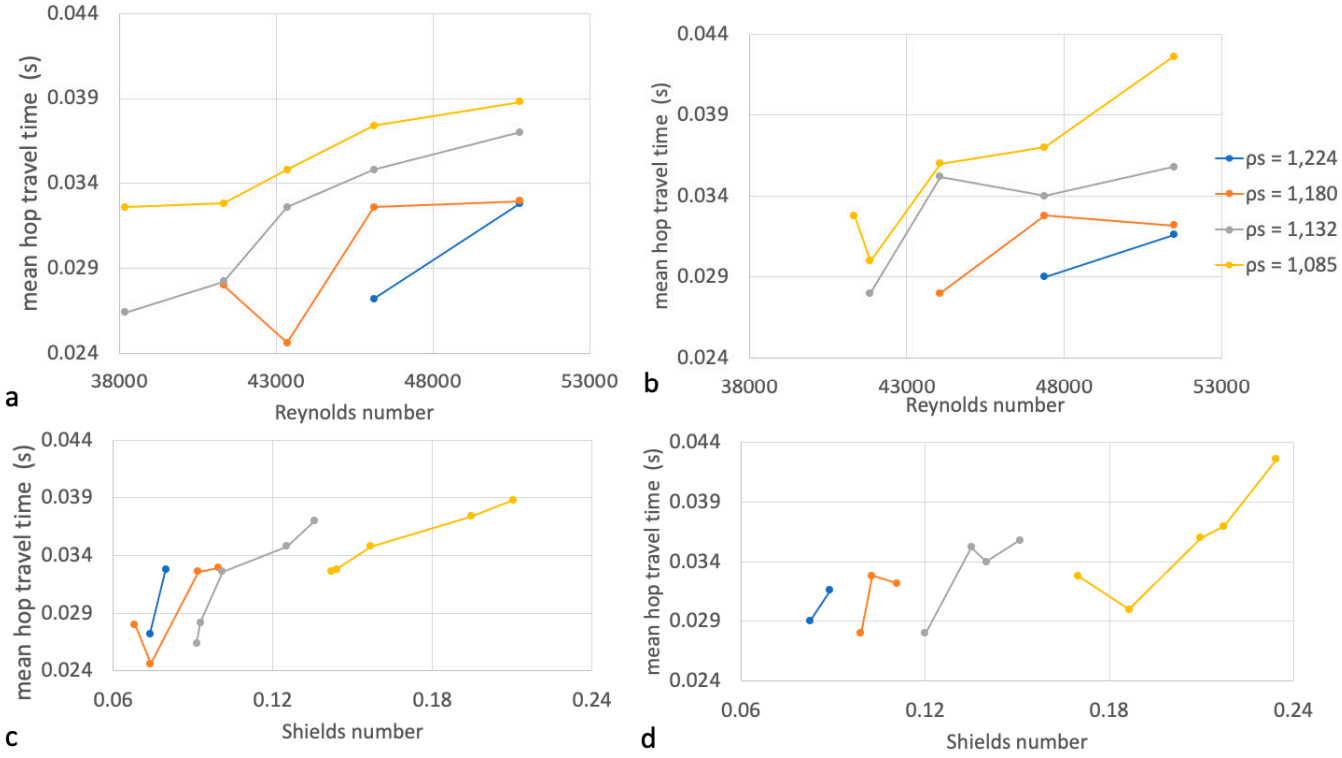

Figure 14. Mean hop travel time for different instrumented particle densities: (**a**) against Reynolds number, for bed surface A, (**b**) against Reynolds number, for bed surface B, (**c**) against Reynolds number, for bed surface A, and (**d**) against Reynolds number, for bed surface B.

Figure 14 shows that for bed surface A, when there is an increase in flow Reynolds number from 38,190 to 50,789, which is about 35%, or an increase in the Shields number by 50% from 0.091 to 0.135, with fixed particle density 1132 kg/m^3, the particle will interact with the bed less and remain for longer durations and there will be an increase in the mean time interval of particle hop, as it increases by 40% from 0.0264 to 0.0370 s.

When the particle density decreases by about 10% from 1180 to 1085 kg/m^3, the mean particle hop travel time will increase by 40% from 0.0246 to 0.0348 s, with fixed flow Reynolds number of 43,353. In addition, particle velocities are low on average, so the net time travel of particle hops are short on average.

For bed surface B, Figure 14 shows clearly that when there is an increase in flow Reynolds number from 44,060 to 51,488, which is about 15%, or an increase in the Shields number of about 10% from 0.099 to 0.111, with fixed particle density 1180 kg/m^3 in bed surface B, the particle will interact with the bed less and remain for longer durations and there will be an increase in the mean time interval of particle hop, which will increase by about 15% from 0.028 to 0.032 s, so there will be higher hopping (saltation length) with lower saltation movements and the average number of hops per second for particle movement decreases.

According to Figure 14c, for a fixed Shields number (assume 0.1), mean hop time increases along with particle density increase (e.g., from density of 1132 to 1180 kg/m^3. Heavier particles respond slower to the same mean driving flow force (e.g., same mean bed shear stresses), leading to the particle having increased times between hop events.

When particle density decreases by about 15% from 1224 to 1085 kg/m^3, the mean particle hop travel time will increase from 0.029 to 0.037 s, which is about 30% with a fixed flow Reynolds number of 47,379 surface B, which shows that the decrease in particle density

results in big changes in particle hop travel time. The travel time of particle movement is short as the particle velocity is short and it increases as particle velocity increases.

In conclusion, Figure 14 shows that the mean time interval of particle hops increases with higher flow velocity or particle velocity and decreases with higher specific density. Thus, with increasing channel flow Reynolds number or decreasing particle density, the particle will interact with the bed less and remain for longer durations and therefore achieve greater hop travel time. With increasing shear velocity, the total duration of the particle in motion will also increase.

4.3. Dependence of Particle Velocity on Particle and Flow Features

Mean streamwise particle velocities can be modelled from fitting exponential distributions of different particle densities and channel flow rates. Below, their interdependence is quantified, and any trends are assessed. Figure 15 shows a comparison of the particle velocity exponential distributions fit to empirical data obtained experimentally from the instrumented particle, for different particle densities and flow Reynolds numbers.

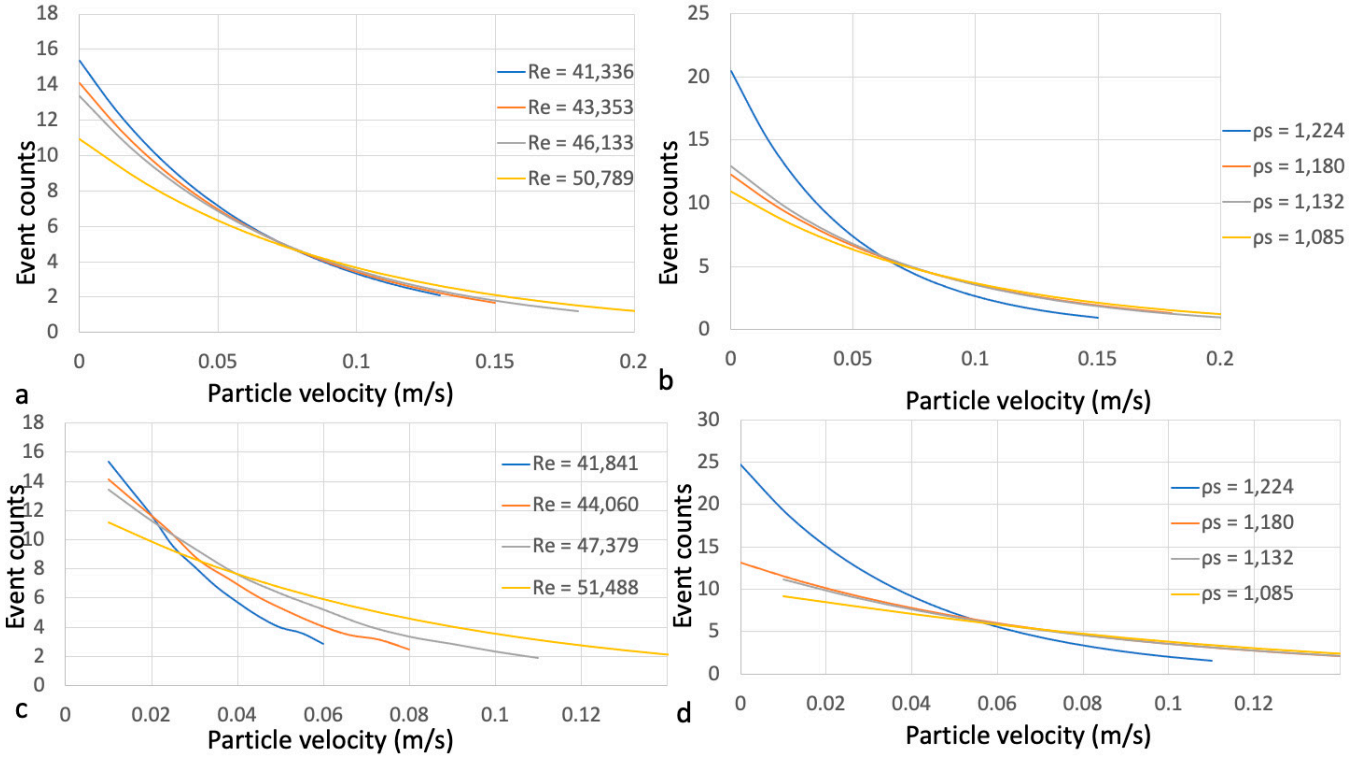

Figure 15. Instrumented particle velocity modelled by the exponential distribution: (**a**) for different flow Reynolds numbers, bed surface A and fixed instrumented particle density of 1132 kg/m^3, (**b**) for different instrumented particle densities, bed surface A and fixed Reynolds number of 50,789, (**c**) for different flow Reynolds numbers, bed surface B and fixed instrumented particle density of 1132 kg/m^3, and (**d**) for different instrumented particle densities, bed surface B and fixed Reynolds number of 51,488.

From Figure 15a,c, it is observed that with increasing flow Reynolds numbers, the probability of occurrence of higher streamwise particle velocity increases for both surfaces. For example, in bed surface A (Figure 15a), when flow Reynolds number increased by 15% from 43,353 to 50,789 the probability of occurrence increased from 3.6 to 3.95, which is about 15% for the same streamwise particle velocity of 0.12 m/s. In addition, as the particle density decreases, transport for the same flow becomes easier and the probability of occurrence of the higher streamwise particle velocity increases for both surfaces. For example, in bed surface B (Figure 15c), when particle density decreased by 15% from

1224 to 1085 kg/m^3, the probability of occurrence increased from 3.81 to 4.25 (50%) for the same streamwise particle velocity of 0.09 m/s.

The point where individual probability distributions meet (each having a different rate of change for particle velocities) indicates the streamwise particle velocity where the distributions are having the same probability of occurrence. This crossing is not clearly distinguishable for many cases, and it is prone to uncertainties in fitting the modelled probability distributions. More distinct are peaks (showing the most commonly occurring particle velocity) and mean of the individual distributions, as well as the extent of their tail (illustrating the magnitude of extreme particle velocities).

The effects of different particle densities and flow Reynolds number on the fitted exponential distribution parameters, modelling instrumented particle velocities, are also tabulated in Tables 6 and 7, offered in Appendix A, along with further discussion, to allow for a clearer representation of the variations in the body and specifically the tail of the distribution (that may be hard to discern in Figure 15).

Figure 16 shows the plot of the effect of different channel flow conditions (i.e., Reynolds and Shields numbers) and test particle densities kg/m^3, from the exponential distribution fittings on the streamwise particle velocity m/s, for bed surfaces A and B. The Shields numbers are used to generalize the results for different combinations of flow and particle conditions.

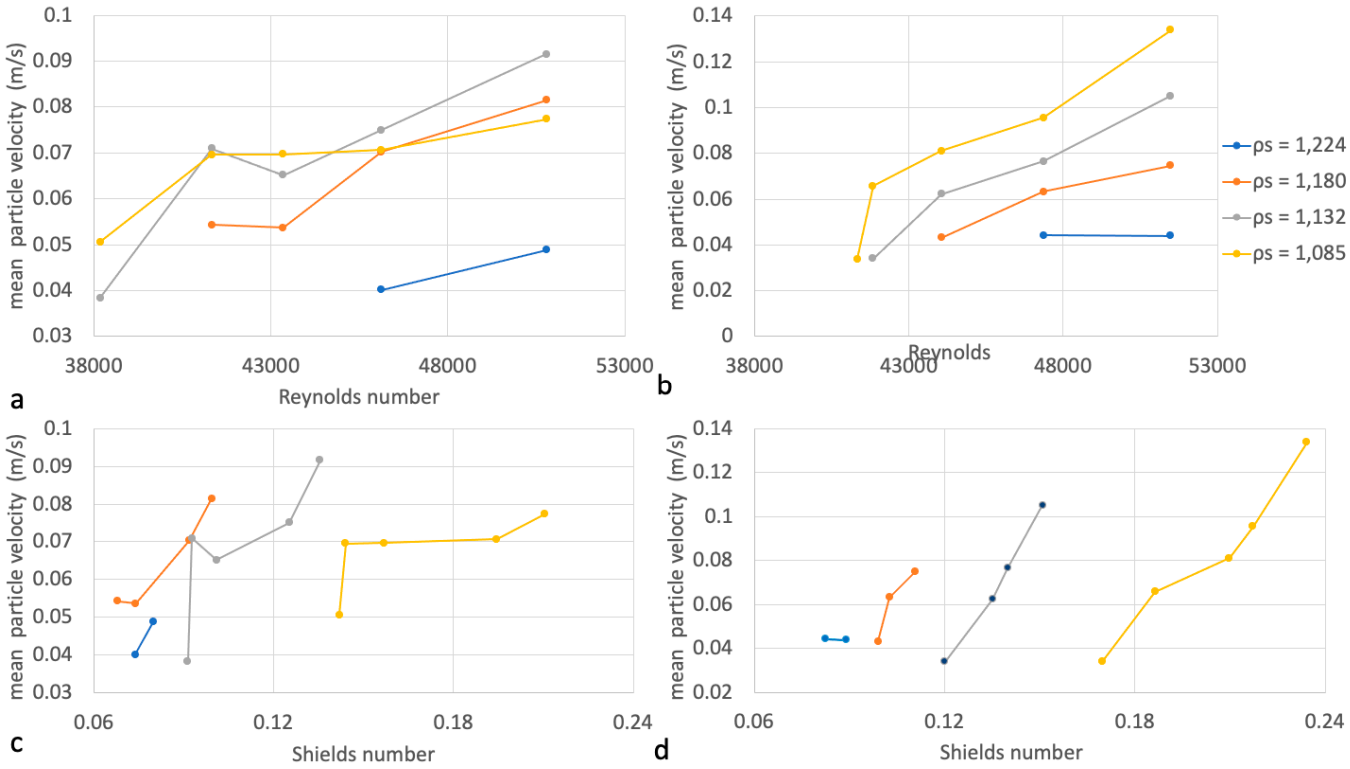

Figure 16. Mean instrumented particle velocity, for different solid densities: (**a**) against Reynolds number, for bed surface A, (**b**) against Reynolds number, for bed surface B, (**c**) against Reynolds number, for bed surface A, and (**d**) against Reynolds number, for bed surface B.

For bed surface A and fixed particle density 1132 kg/m^3 (Figure 16a), with a ~35% increase in flow Reynolds number (from 38,190 to 50,789, or an equivalent 50% increase in the Shields number, from 0.09 to 0.135—Figure 16c), the particle will interact with the bed surface less and move for longer hop lengths (consistent to what is shown in Figure 12a,c, and Figure 14a,c, respectively), resulting in a ~140% increase in mean particle velocity (from 0.038 to 0.092 m/s). For a 10% decrease in particle density (from 1180 to 1085 kg/m^3), mean particle velocity will increase by 30% (from 0.054 to 0.07 m/s) with

fixed flow Reynolds number of 43,353, and the net time travel of particle hops will increase on average. Similarly, for bed surface B and fixed particle density 1180 kg/m^3 (Figure 16b), with a ~15% increase in flow Reynolds number from 44,060 to 51,488, (or an increase of 10% in the Shields number from 0.099 to 0.111, Figure 16d), for bed surface B, there will be increase in the mean particle velocity from 0.043 to 0.075 m/s (75%). There will be higher hopping (saltation) length and the average number of hops per second decreases, and with an increase in shear velocity, the mean particle velocity m/s will also increase. For fixed flow Reynolds number of 47,379 and bed surface B (Figure 16c), with a particle density that decreases by about 15% (from 1224 to 1085 kg/m^3), mean particle velocity will increase by 115% (from 0.044 to 0.095 m/s), which shows how lighter particles are transported faster.

4.4. Considerations around the Instrumented Particle's Design

The instrumented particle presented herein is a novel sensing equipment for the study of bedload transport of particles. The results of this study and derived distribution models are accurate and can be used directly for parameterizing the transport of solid particles that are lighter than sediment. This can find a host of modern direct eco-hydraulic and engineering applications, including habitat assessment and monitoring [68] as well as transport of plastics through the fluvial vector, which are emerging research fields. These results are also directly applicable in helping further identify, also for the first time, trends in the dynamics of particle transport and their interaction with the bed surface, for a range of assessed parameters, including (a) solid particle density, (b) bed surface roughness, and (c) flow conditions, above threshold. These are of great importance for computational fluid dynamics and discrete element modelers (CFD-DEM, e.g., [21]), which can use such stochastic models to match any coefficients behind their constitutive or particle micromechanical models and validate them.

The size and shape of the instrumented particle are selected so that for the range of flow conditions trialed herein, a range of solid transport rates above threshold can be achieved. A fully spherical particle allows for a relatively higher transport rate for the same flow conditions. The particle size is miniaturized to scales comparable to natural sediment particles (of diameter <80 mm, e.g., large, rounded pebbles). Future research may focus on particle shapes to study the dependence of particle transport dynamics on different shapes, following the same design of experiments and framework of analysis as shown here. Typically, the instrumented particle's casing size is limited by the IMU sensor's size, but this can be further miniaturized with custom designed electronics and sensor calibration routines, as shown recently [48], enabling assessing trends for a wider range of transported particle properties. Despite these differences to natural sediment particles, the mode of transport by saltation as well as the modeling of distributions of a range of metrics used to assess it are found to be comparable to what other researchers have found for natural sediment particles.

The instrumented particle used in this study addresses limitations of active or passive tracer methods [69–72] such as inaccessibility, high initial purchase and deployment costs, low recovery rates (due to different deployment methods), as well as requirements for professional labor to apply the technique. It is a robust, stepper-like device that can offer advanced insights for the dynamics of bedload transport. An improved understanding of sediment transport dynamics can be obtained by analyzing the flow forces acting on individual sediment particles near the channel bed surface, under certain hydraulic and hydrodynamic conditions towards enabling more robust assessment of the geomorphic processes and allowing for adopting improved sediment management strategies and water resources planning [38,73].

5. Conclusions

It is shown that the instrumented particles can be a useful tool in providing a better understanding of how local hydrodynamic conditions may instantaneously induce different particle interactions with the bed surface, affecting its transport features, and enable a

deeper understanding of the diversity of complex bed load sediment transport dynamics, especially at above-threshold transport conditions. In general, the assessed trends are in accordance with literature findings, and the results obtained from the instrumented particle for a range of experimental parameters demonstrate a novel robust tool as well as framework for using it and analyzing its data towards a probabilistic modeling of bedload processes that has a significant potential for offering new insights for the dynamics of these processes for physical and numerical modelers.

The mean hop length, hop travel time, and streamwise particle velocities values were obtained by using the goodness of fit for different probabilistic distributions for all the performed experiments with varying flow rates and particle density under equilibrium transport conditions. It was found that hop travel times, hop length, and mean streamwise particle velocities are best modelled with the exponential, Gamma, and exponential distributions, respectively. By increasing hydrodynamic forcing near the bed surface (assessed with Reynolds and Shields numbers) or decreasing instrumented particle density, the particle will have fewer occurrences of interacting with the bed surface (number of hops) and will transverse the same distance along the channel's bed surface in a shorter time, and with higher instantaneous particle velocities.

Author Contributions: Conceptualization, M.V.; Data curation, Z.A.; Formal analysis, Z.A.; Funding acquisition, M.V.; Investigation, Z.A. and M.V.; Methodology, Z.A. and M.V.; Project administration, M.V.; Software, Z.A.; Supervision, M.V.; Validation, Z.A. and M.V.; Visualization, Z.A. and M.V.; Writing—original draft, Z.A. and M.V.; Writing—review and editing, Z.A. and M.V. All authors have read and agreed to the published version of the manuscript.

Funding: This research was supported by the Royal Society (Research Grant RG2015 R1 68793/1) and the Royal Society of Edinburgh (Crucible Award).

Institutional Review Board Statement: Not applicable.

Informed Consent Statement: Not applicable.

Data Availability Statement: Data used in this study are available in tabulated form in the manuscript (in the main text and the Appendix A).

Acknowledgments: The authors would like to thank Thanos Alexakis for helping with the design of instrumented particle casing and are grateful to the reviewers for their useful remarks.

Conflicts of Interest: The authors declare no conflict of interest.

Appendix A

Appendix A.1 Dependence of Hop Distances on Particle and Flow Features

From Table 1, the probability of occurrence of the longest hop lengths increases with decreasing particle density. For example, for bed surface A with fixed Reynolds number of 50,789, the probability of occurrence for high lengths (>0.01 m) increased from 0.4% to 4.1% when the particle density decreased from 1224 to 1085 kg/m^3. Inversely, the probability of occurrence of low hop lengths (0–0.0025 m increased from 43.4% to 65.7% when the particle density increased from 1085 to 1180 kg/m^3 for bed surface B with fixed Reynolds number of 51,488.

Table A1. The effect of different particle densities on the hop distance Gamma distribution model parameters, for bed surface A (and Reynolds number of 50,789), and bed surface B (and Reynolds number of 51,488). These tabulated data correspond to the results plotted in Figure 11b,d.

	Surface A				**Surface B**			
	Particle Density (kg/m^3)				**Particle Density (kg/m^3)**			
	1085	**1132**	**1180**	**1224**	**1085**	**1132**	**1180**	**1224**
Hop Length (m)	**Probability of Occurrence (%)**							
0–0.0025	47.1	65.79	67.4	67.6	43.4	65.84	65.7	69.1
0.0025–0.005	28.8	22.55	22.6	23.4	30.1	22.56	25.4	21.9
0.005–0.0075	13.9	7.69	7.0	6.9	15.2	7.57	6.4	6.9
0.0075–0.01	6.1	2.62	2.1	1.6	6.7	2.60	1.8	1.6
>0.01	4.1	1.34	0.9	0.4	4.5	1.32	0.7	0.4

From Table 2, the probability of occurrence of high hop lengths increases with increasing flow Reynolds number, while for low hop lengths, it decreases with an increase in flow Reynolds number for fixed particle density of 1132 kg/m^3. For example, the probability of occurrence of low hop lengths 0–0.0025 m decreased from 66.6% to 65.8% when the flow Reynolds number increased from 41,337 to 46,133 (for bed surface A with fixed particle density of 1132 kg/m^3). The probability of occurrence for high hop distances 0.0075–0.01 m increased from 1.4% to 8% when the flow Reynolds number increased from 41,841 to 51,488, for the case of fixed particle density of 1132 kg/m^3 and bed surface B.

Table A2. The effect of different flow Reynolds numbers on the hop distance Gamma distribution model parameters, for bed surfaces A and B, for fixed particle density of 1132 kg/m^3. These tabulated data correspond to the results plotted in Figure 11a,c.

	Surface A				**Surface B**			
	Flow Reynolds Number				**Flow Reynolds Number**			
	41,337	**43,353**	**46,133**	**50,789**	**41,841**	**44,060**	**47,379**	**51,488**
Hop Length (m)	**Probability of Occurrence (%)**							
0–0.0025	66.6	66.3	65.8	57.4	64.8	65.3	65.8	37.0
0.0025–0.005	25.4	25.1	22.9	27.7	25.8	25.1	22.6	32.1
0.005–0.0075	6.4	6.7	7.5	10.1	7.6	7.3	7.7	17.6
0.0075–0.01	1.4	1.5	2.6	3.4	1.4	1.6	2.6	8.0
>0.01	0.3	0.4	1.3	1.3	0.4	0.6	1.3	5.3

Appendix A.2 Dependence of Hop Travel Time on Particle and Flow Features

From Table 3 with fixed flow Reynolds numbers, the probability of occurrence of high hop travel times increases with a decrease in the particle density. For example, the probability of occurrence of high hop travel time 0.08–0.09 s increased from 1.3% to 1.9% when the particle density decreased from 1180 to 1085 kg/m^3, Reynolds number of 50,789, for bed surface A. The probability of occurrence for low hop travel times (e.g., 0.01–0.02 s) increased from 20.2% to 23.1%, when the particle's density increased from 1085 to 1224 kg/m^3, for bed surface B and a fixed Reynolds number of 51,488.

Table A3. The effect of different particle densities on the travel time exponential distribution model parameters, for bed surface A (and Reynolds number of 50,789), and bed surface B (and Reynolds number of 51,488). These tabulated data correspond to the results plotted in Figure 13b,d.

	Surface A				**Surface B**			
	Particle Density (kg/m^3)				**Particle Density (kg/m^3)**			
	1085	**1132**	**1180**	**1224**	**1085**	**1132**	**1180**	**1224**
Hop Travel Time (s)	**Probability of Occurrence (%)**							
0–0.01	30.8	31.9	34.8	35.1	27.4	32.9	35.2	36.0
0.01–0.02	21.5	21.9	22.8	22.9	20.2	22.0	22.5	23.1
0.02–0.03	15.0	15.0	14.9	14.9	14.8	15.0	15.0	14.9
0.03–0.04	10.5	10.3	9.8	9.7	10.9	10.1	9.7	9.6
0.04–0.05	7.3	7.1	6.4	6.4	8.0	6.8	6.3	6.2
0.05–0.06	5.1	4.9	4.2	4.2	5.9	4.6	4.2	4.0
0.06–0.07	3.8	3.5	2.9	2.8	4.6	3.5	2.9	2.7
0.07–0.08	2.7	2.5	1.9	1.9	3.5	2.3	2.0	1.8
0.08–0.09	1.9	1.7	1.3	1.3	2.6	1.6	1.3	1.2
0.09–0.10	1.4	1.3	0.9	0.9	2.0	1.1	0.9	0.8

From Table 4, the probability of occurrence of high hop travel times increases with increasing flow Reynolds number while the probability for low hop travel time decreases with increasing flow Reynolds numbers, for a fixed particle density of 1132 kg/m^3. For example, the probability of occurrence for relatively shorter hop travel times (0–0.01 s) decreased from 35.3% to 31.9% when the flow Reynolds number increased from 41,841 to 51,488, for bed surface B with fixed particle density of 1132 kg/m^3. The probability of occurrence of longer hop travel time (0.08–0.09 s) increased from 1.2% to 1.5% when the flow Reynolds number increased from 41,337 to 46,133 with fixed particle density of 1132 kg/m^3 for bed surface A.

Table A4. The effect of different flow Reynolds numbers on the travel time exponential distribution model parameters, for bed surfaces A and B, for fixed particle density of 1132 kg/m^3. These tabulated data correspond to the results plotted in Figure 13a,c.

	Surface A				**Surface B**			
	Flow Reynolds Number				**Flow Reynolds Number**			
	41,337	**43,353**	**46,133**	**50,789**	**41,841**	**44,060**	**47,379**	**51,488**
Hop Travel Time (s)	**Probability of Occurrence (%)**							
0–0.01	35.6	34.2	33.4	32.9	35.3	35.1	33.7	31.9
0.01–0.02	23.0	22.6	22.4	22.0	23.0	22.9	22.5	21.9
0.02–0.03	14.9	15.0	15.0	15.0	14.9	14.9	15.0	15.0
0.03–0.04	9.6	9.9	10.0	10.1	9.7	9.7	10.0	10.3
0.04–0.05	6.2	6.6	6.7	6.8	6.3	6.4	6.7	7.1
0.05–0.06	4.0	4.3	4.5	4.6	4.1	4.1	4.5	4.9
0.06–0.07	2.7	3.0	3.2	3.5	2.8	2.8	3.1	3.5
0.07–0.08	1.8	2.0	2.2	2.3	1.8	1.9	2.1	2.5
0.08–0.09	1.2	1.4	1.5	1.6	1.2	1.3	1.5	1.7
0.09–0.10	0.8	1.0	1.1	1.1	0.8	0.9	1.0	1.3

Appendix A.3 Dependence of Particle Velocity on Particle and Flow Features

From Table 5 with fixed flow rates (Reynolds number), the probability of occurrence of high particle velocities increases with decrease in the particle density. For example, the probability of occurrence for high particle velocities (0.15–0.165 m/s) increased from 1.8% to 2.6% when the particle density decreased from 1224 to 1132 kg/m^3 with fixed Reynolds number of 50,789 for bed surface A. Meanwhile, the probability of occurrence for low particle velocities (0–0.015 m/s) increased from 17.3% to 25.1% when the particle density increased from 1085 to 1224 kg/m^3 for bed surface B with fixed Reynolds number of 51,499.

Table A5. The effect of different particle densities on the particle velocity exponential distribution model parameters, for bed surface A (and Reynolds number of 50,789), and bed surface B (and Reynolds number of 51,488). These tabulated data correspond to the results plotted in Figure 15b,d.

	Surface A				**Surface B**			
	Particle Density (kg/m^3)				**Particle Density (kg/m^3)**			
	1085	**1132**	**1180**	**1224**	**1085**	**1132**	**1180**	**1224**
Hop Velocity (m/s)	**Probability of Occurrence (%)**							
0–0.015	20.3	21.1	23.0	24.4	17.3	19.3	20.6	25.1
0.015–0.03	16.7	17.1	18.1	18.8	15.5	16.1	16.8	19.1
0.03–0.045	13.7	13.8	14.2	14.5	13.3	13.4	13.7	14.6
0.045–0.06	11.2	11.2	11.2	11.1	11.4	11.1	11.2	11.1
0.06–0.075	9.2	9.1	8.8	8.6	9.9	9.3	9.1	8.5
0.075–0.09	7.5	7.3	6.9	6.6	8.3	7.7	7.5	6.4
0.09–0.105	6.2	5.9	5.4	5.1	6.9	6.4	6.1	4.9
0.105–0.12	5.0	4.8	4.3	3.9	5.7	5.3	5.0	3.7
0.12–0.135	4.1	3.9	3.4	3.0	4.7	4.5	4.0	2.8
0.135–0.15	3.4	3.2	2.7	2.3	3.8	3.7	3.3	2.2
0.15–0.165	2.8	2.6	2.1	1.8	3.1	3.1	2.7	1.7

From Table 6, the probability of occurrence for high particle velocities increases with increase in the flow Reynolds number while for low particle velocities it increases with decrease in flow Reynolds number for fixed particle density of 1132 kg/m^3. For example, the probability of occurrence for low particle velocities (0–0.015 m/s) decreased from 27.4% to 21.7% when the flow Reynolds number increased from 43,353 to 50,789 for bed surface A with fixed particle density of 1132 kg/m^3. While the probability of occurrence for high particle velocities (0.15–0.165 m/s) increased from 2.7% to 3.3% when the flow Reynolds number increased from 41,841 to 51,488 with fixed particle density of 1132 kg/m^3 for bed surface B.

In Table 7, the flow conditions tested herein are also reported in terms of the particle Reynolds number for enabling further comparisons with the literature. This is important to assess, as sometimes a change in the near bed surface hydrodynamic forcing, may not be reflected in the change in flow Reynolds number (for example if the tailgate was raised while keeping the flow rate constant). In this case the Re number may be almost fixed while the particle Reynolds number may decrease, with a potential to also affect the transport rates.

Table A6. The effect of different flow Reynolds numbers on the particle velocity exponential distribution model parameters, for bed surfaces A and B, for fixed particle density of 1132 kg/m^3. These tabulated data correspond to the results plotted in Figure 15a,c.

	Surface A				**Surface B**			
	Flow Reynolds Number				**Flow Reynolds Number**			
	41,337	**43,353**	**46,133**	**50,789**	**41,841**	**44,060**	**47,379**	**51,488**
Hop Velocity (m/s)	**Probability of Occurrence (%)**							
0–0.015	27.6	27.4	24.4	21.7	20.6	19.8	18.3	17.9
0.015–0.03	20.2	20.1	18.8	17.4	16.8	16.6	16.0	15.7
0.03–0.045	14.8	14.8	14.5	14.0	13.7	13.8	13.7	13.6
0.045–0.06	10.9	10.9	11.1	11.2	11.2	11.2	11.1	11.1
0.06–0.075	8.0	8.0	8.6	9.0	9.1	9.3	9.4	9.5
0.075–0.09	5.8	5.9	6.6	7.2	7.5	7.7	7.8	7.9
0.09–0.105	4.3	4.3	5.1	5.8	6.1	6.1	6.5	6.6
0.105–0.12	3.1	3.2	3.9	4.6	5.0	5.0	5.4	5.5
0.12–0.135	2.3	2.3	3.0	3.7	4.0	4.2	4.5	4.6
0.135–0.15	1.7	1.7	2.3	3.0	3.3	3.5	4.1	4.2
0.15–0.165	1.2	1.3	1.8	2.4	2.7	2.8	3.2	3.3

Table A7. Relevance of flow and particle Reynolds numbers.

	Surface A				**Surface B**			
Flow Reynolds number (*Re*)	41,337	43,353	46,133	50,789	41,841	44,060	47,379	51,488
Particle Reynolds number (Re_*)	6149	6417	6337	7433	6995	7420	7552	7142

References

1. Buffington, J.; Montgomery, D. A systematic analysis of eight decades of incipient motion studies, with special reference to gravel-bedded rivers. *Water Resour. Res.* **1997**, *33*, 1993–2029. [CrossRef]
2. Pähtz, T.; Clark, A.H.; Valyrakis, M.; Durán, O. The Physics of Sediment Transport Initiation, Cessation, and Entrainment across Aeolian and Fluvial Environments. *Rev. Geophys.* **2020**, *58*, 1–58. [CrossRef]
3. Bagnold, R.A. An approach to the sediment transport problem from general physics. *Physiogr. Hydraul. Stud. Rivers Geol. Surv. Prof. Pap.* **1966**, *422-I*, 1–37.
4. Bagnold, R.A. Transport of solids by natural water flow: Evidence for a worldwide correlation. *Proc. R. Soc. Lond. A Math. Phys. Sci.* **1986**, *405*, 369–374.
5. Gomez, B.; Church, M. An assessment of bed load sediment transport formulae for gravel bed rivers. *Water Resour. Res.* **1989**, *25*, 1161–1186. [CrossRef]
6. Ancey, C.; Davison, A.C.; Böhm, T.; Jodeau, M.; Frey, P. Entrainment and motion of coarse particles in a shallow water stream down a steep slope. *J. Fluid Mech.* **2008**, *595*, 83–114. [CrossRef]
7. Gimenez-Curto, L.A.; Corniero, M.A. Entrainment threshold of cohesionless sediment grains under steady flow of air and water. *Sedimentology* **2009**, *56*, 493–509. [CrossRef]
8. Wilberg, P.L.; Smith, J.D. Model for calculating bed load transport of sediment. *J. Hydraul. Eng.* **1989**, *115*, 101–123. [CrossRef]
9. Bose, S.T.; Dey, S. Sediment Entrainment Probability and Threshold of Sediment Suspension: Exponential-Based Approach. *J. Hydraul. Eng.* **2013**, *139*, 1099–1106. [CrossRef]
10. Török, G.T.; Józsa, J.; Baranya, S. A Shear Reynolds Number-Based Classification Method of the Nonuniform Bed Load Transport. *Water* **2019**, *11*, 73. [CrossRef]
11. Xiao-Hu, Z.; Valyrakis, M.; Zhen-Shan, L. Rock and roll: Incipient aeolian entrainment of coarse particles. *Phys. Fluids* **2021**, *33*, 075117. [CrossRef]
12. Valyrakis, M.; Diplas, P.; Dancey, C.L.; Greer, K.; Celik, A.O. Role of instantaneous force magnitude and duration on particle entrainment. *J. Geophys. Res. Earth Surf.* **2010**, *115*, 1–18. [CrossRef]
13. Valyrakis, M.; Diplas, P.; Dancey, C.L. Entrainment of coarse grains in turbulent flows: An extreme value theory approach. *Water Resour. Res.* **2011**, *47*, 1–17. [CrossRef]

14. Valyrakis, M.; Diplas, P.; Dancey, C.L. Entrainment of coarse particles in turbulent flows: An energy approach. *J. Geophys. Res. Earth Surf.* **2013**, *118*, 42–53. [CrossRef]
15. Ali, S.Z.; Dey, S. Hydrodynamic instability of meandering channels. *Phys. Fluids* **2017**, *29*, 125107. [CrossRef]
16. Van Rijn, L.C. Sediment transport, part I: Bed load transport. *J. Hydraul. Eng.* **1984**, *110*, 1431–1456. [CrossRef]
17. Garcia, C.; Cohen, H.; Reid, I.; Rovira, A.; Úbeda, X.; Laronne, J.B. Processes of initiation of motion leading to bed load transport in gravel-bed rivers. *Geophys. Res. Lett.* **2007**, *34*. [CrossRef]
18. Drake, T.G.; Shreve, R.L.; Dietrich, W.E.; Whiting, P.J.; Leopold, L.B. Bed load transport of fine gravel observed by motion-picture photography. *J. Fluid Mech.* **1988**, *192*, 193–217. [CrossRef]
19. Cecchetto, M.; Tregnaghi, M.; Bottacin-Busolin, A.; Tait, S.; Marion, A. Statistical description on the role of turbulence and grain interference on particle entrainment from gravel beds. *J. Hydraul. Eng.* **2017**, *143*, 06016021. [CrossRef]
20. Coleman, N. A theoretical and experimental study of drag and lift forces acting on a sphere resting on a hypothetical streambed. In Proceedings of the 12th Congress of International Association for Hydraulic Research, Fort Collins, CO, USA, 11–14 September 1967.
21. Schmeeckle, M.W.; Nelson, J.M.; Shreve, R.L. Forces on stationary particles in near-bed turbulent flows. *J. Geophys. Res. Earth Surf.* **2007**, *112*, 1–21. [CrossRef]
22. Diplas, P.; Dancey, C.L.; Celik, A.O.; Valyrakis, M.; Greer, K.; Akar, T. The Role of Impulse on the Initiation of Particle Movement under Turbulent Flow Conditions. *Science* **2008**, *322*, 717–720. [CrossRef]
23. Hofland, B.; Battjes, J.A.; Booij, R. Measurement of fluctuating pressures on coarse bed material. *J. Hydraul. Eng.* **2005**, *131*, 770–781. [CrossRef]
24. Jeffreys, H. On the transport of sediments by streams. *Math. Proc. Phil. Soc.* **1929**, *25*, 272–276. [CrossRef]
25. Iwagaki, Y. (I) Hydrodynamical study on critical tractive force. *Trans. Jpn. Soc. Civ. Eng.* **1956**, *41*, 1–21. [CrossRef]
26. Wiberg, P.L.; Smith, J.D. Calculations of the critical shear stress for motion of uniform and heterogeneous sediments. *Water Resour. Res.* **1987**, *23*, 1471–1480. [CrossRef]
27. Hofland, B.; Battjes, J. Probability density function of instantaneous drag forces and shear stresses on a bed. *J. Hydraul. Eng.* **2006**, *132*, 1169–1175. [CrossRef]
28. Campagnol, J.; Radice, A.; Ballio, F.; Nikora, V. Particle motion and diffusion at weak bed load: Accounting for unsteadiness effects of entrainment and disentrainment. *J. Hydraul. Res.* **2015**, *53*, 633–648. [CrossRef]
29. Fathel, S.L.; Furbish, D.J.; Schmeeckle, M.W. Experimental evidence of statistical ensemble behavior in bed load sediment transport. *J. Geophys. Res. Earth Surf.* **2015**, *120*, 2298–2317. [CrossRef]
30. Furbish, D.J.; Schmeeckle, M.W.; Schumer, R.; Fathel, S.L. Probability distributions of bed load particle velocities, accelerations, hop distances, and travel times informed by Jaynes's principle of maximum entropy. *J. Geophys. Res. Earth Surf.* **2016**, *121*, 1373–1390. [CrossRef]
31. Lajeunesse, E.; Malverti, L.; Charru, F. Bed load transport in turbulent flow at the grain scale: Experiments and modeling. *J. Geophys. Res. Earth Surf.* **2010**, *115*. [CrossRef]
32. Liu, D.; Valyrakis, M.; Williams, R. Flow Hydrodynamics across Open Channel Flows with Riparian Zones: Implications for Riverbank Stability. *Water* **2017**, *9*, 720. [CrossRef]
33. Nasrollahi, A.; Ghodsian, M.; Neyshabouri, S. Local scour at permeable spur dikes. *Appl. Sci.* **2008**, *8*, 3398–3406. [CrossRef]
34. Izadinia, E.; Heidarpour, M.; Schleiss, A. Investigation of turbulence flow and sediment entrainment around a bridge pier. *Stoch. Environ. Res. Risk Assess.* **2012**, *27*, 1303–1314. [CrossRef]
35. Michalis, P.; Tarantino, A.; Tachtatzis, C.; Judd, D.M. Wireless Monitoring of Scour and Re-deposited Sediment Evolution at Bridge Foundations based on Soil Electromagnetic Properties. *Smart Mater. Struct.* **2015**, *24*, 1–15. [CrossRef]
36. Pandey, M.; Valyrakis, M.; Qi, M.; Sharma, A.; Lodhi, A.S. Experimental assessment and prediction of temporal scour depth around a spur dike. *Int. J. Sed. Res.* **2020**, *36*, 17–28. [CrossRef]
37. Papanicolaou, A.; Diplas, P.; Evaggelopoulos, N.; Fotopoulos, S. Stochastic incipient motion criterion for spheres under various bed packing conditions. *J. Hydraul. Eng.* **2002**, *128*, 369–380. [CrossRef]
38. Hassan, M.A.; Voepel, H.; Schumer, R.; Parker, G.; Fraccarollo, L. Displacement characteristics of coarse fluvial bed sediment. *J. Geophys. Res. Earth Surf.* **2013**, *118*, 155–165. [CrossRef]
39. Akeila, E.; Salcic, Z.; Kularatna, N.; Melville, B.; Dwivedi, A. Testing and calibration of smart pebble for river bed sediment transport monitoring. In Proceedings of the IEEE Sensors, Atlanta Georgia, GA, USA, 28–31 October 2007.
40. Akeila, E.; Salcic, Z. Smart Pebble for Monitoring Riverbed Sediment Transport. *IEEE Sens.* **2010**, *10*, 1705–1717. [CrossRef]
41. Kularatnal, N.; Kularatna-Abeywardana, D. Use of motion sensors for autonomous monitoring of hydraulic environments. In Proceedings of the IEEE Sensors, Lecce, Italy, 26–29 October 2008.
42. Gronz, O.; Hiller, P.; Wirtz, S.; Becker, K.; Iserloh, T.; Seeger, M.; Brings, C.; Aberle, J.; Casper, M.; Ries, J. Smartstones: A small 9-axis sensor implanted in stones to track their movements. *Catena* **2016**, *142*, 245–251. [CrossRef]
43. Frank, D.; Foster, D.; Sou, I.; Calantoni, J.; Chou, P. Lagrangian measurements of incipient motion in oscillatory flows. *J. Geophys. Res. Ocean.* **2014**, *120*, 244–256. [CrossRef]
44. Maniatis, G.; Hoey, T.; Hassan, M.; Sventek, J.; Hodge, R.; Drysdale, T.; Valyrakis, M. Calculating the Explicit Probability of Entrainment Based on Inertial Acceleration Measurements. *J. Hydraul. Eng.* **2017**, *143*, 1–43. [CrossRef]

45. Noss, C.; Koca, K.; Zinke, P.; Henry, P.H.; Navaratnam, C.U.; Aberle, J.; Lorke, A. A Lagrangian drifter for surveys of water surface roughness in streams. *J. Hydraul. Res.* **2019**, *58*, 471–488. [CrossRef]
46. Valyrakis, M.; Alexakis, A. Development of a "smart-pebble" for tracking sediment transport. In Proceedings of the International Conference on Fluvial Hydraulics, St. Louis, MO, USA, 12–15 July 2016.
47. Al-Obaidi, K.; Xu, Y.; Valyrakis, M. The Design and Calibration of Instrumented Particles for Assessing Water Infrastructure Hazards. *J. Sens. Actuat. Netw.* **2020**, *9*, 36. [CrossRef]
48. Al-Obaidi, K.; Valyrakis, M. A sensory instrumented particle for environmental monitoring applications: Development and calibration. *IEEE Sens. J.* **2021**, *21*, 10153–10166. [CrossRef]
49. AlObaidi, K.; Valyrakis, M. Explicit linking the probability of entrainment to the flow hydrodynamics. *Earth Surface Process. Landf.* **2021**. [CrossRef]
50. Bohorquez, P.; Ancey, C. Stochastic-deterministic modeling of bed load transport in shallow water flow over erodible slope: Linear stability analysis and numerical simulation. *Adv. Water Resour.* **2015**, *83*, 36–54. [CrossRef]
51. Einstein, H.A. Bedload Transport as a Probability Problem. Ph.D. Thesis, ETH Zurich, Zurich, Switzerland, 1937.
52. Yang, C.T.; Sayre, W.W. Stochastic model for sand dispersion. *J. Hydraul. Div. ASCE* **1971**, *97*, 265–288. [CrossRef]
53. Bagnold, R.A. The nature of saltation and of 'bed-load'transport in water. *Proc. R. Soc. Lond. A Math. Phys. Sci.* **1973**, *332*, 473–504.
54. Shields, A. *Application of Similarity Principles and Turbulence Research to Bed-Load Movement*; California Institute of Technology: Pasadena, CA, USA, 1936.
55. Towsend, A.A. *The Structure of Turbulent Shear Flow*, 2nd ed.; The Press Syndicate of the University of Cambridge: Cambridge, UK, 1980.
56. Papanicolaou, T.; Knapp, D. A particle tracking technique for bedload motion. In Proceedings of the 7th International Conference on HydroScience and Engineering, Philadelphia, PA, USA, 10–13 September 2006.
57. Ballio, F.; Pokrajac, D.; Radice, A.; Hosseini-Sadabadi, S.A. Lagrangian and Eulerian description of bed load transport. *J. Geophys. Res. Earth Surf.* **2018**, *123*, 384–408. [CrossRef]
58. Roseberry, J.C.; Schmeeckle, M.W.; Furbish, D.J. A probabilistic description of the bed load sediment flux: 2. Particle activity and motions. *J. Geophys. Res. Earth Surf.* **2012**, *117*. [CrossRef]
59. Schmidt, K.H.; Ergenzinger, P. Bed load entrainment, travel lengths, step lengths, rest periods—Studied with passive (iron, magnetic) and active (radio) tracer techniques. *Earth Surf. Proc. Landf.* **1992**, *17*, 147–165. [CrossRef]
60. Lamarre, H.; Roy, A.G. A field experiment on the development of sedimentary structures in a gravel-bed river. *Earth Surf. Proc. Landf.* **2008**, *33*, 1064–1081. [CrossRef]
61. Hassan, M.A.; Church, M.; Schick, A.P. Distance of movement of coarse particles in gravel bed streams. *Water Resour. Res.* **1991**, *27*, 503–511. [CrossRef]
62. Habersack, H. Radio-tracking gravel particles in a large braided river in New Zealand: A field test of the stochastic theory of bed load transport proposed by Einstein. *Hydrol. Proc.* **2001**, *15*, 377–391. [CrossRef]
63. Nakagawa, H.; Tsujimoto, T. Sand bed instability due to bed load motion. *J. Hydraul. Div. ASCE* **1980**, *106*, 2029–2051. [CrossRef]
64. Martin, R.L.; Jerolmack, D.J.; Schumer, R. The physical basis for anomalous diffusion in bed load transport. *J. Geophys. Res. Earth Surf.* **2012**, *117*. [CrossRef]
65. Ancey, C.; Heyman, J. A microstructural approach to bed load transport: Mean behaviour and fluctuations of particle transport rates. *J. Fluid Mech.* **2014**, *744*, 129–168. [CrossRef]
66. Heays, K.; Friedrich, H.; Melville, B.; Nokes, R. Quantifying the dynamic evolution of graded gravel beds using particle tracking velocimetry. *J. Hydraul. Eng.* **2014**, *140*, 04014027. [CrossRef]
67. Hosseini-Sadabadi, S.A. Langragian and Eulerian Study of Bed-Load Kinematics. Ph.D. Thesis, Politecnico di Milano, Milan, Italy, 2017.
68. Curley, E.A.M.; Valyrakis, M.; Thomas, R.; Adams, C.E.; Stephen, A. Smart sensors to predict entrainment of freshwater mussels: A new tool in freshwater habitat assessment. *Sci. Total Environ.* **2021**, *787*, 1–11. [CrossRef]
69. Nichols, M. A radio frequency identification system for monitoring coarse sediment particle displacement. *Appl. Eng. Agric.* **2004**, *20*. [CrossRef]
70. MacVicar, B.J.; Piégay, H.; Henderson, A.; Comiti, F.; Oberlin, C.; Pecorari, E. Quantifying the temporal dynamics of wood in large rivers: Field trials of wood surveying, dating, tracking, and monitoring techniques. *Earth Surf. Proc. Landf.* **2009**, *34*, 2031–2046. [CrossRef]
71. Liébault, F.; Hervé, B.; Chapuis, M.; Klotz, S.; Deschâtres, M. Bedload tracing in a high-sediment-load mountain stream. *Earth Surf. Proc. Landf.* **2011**, *37*, 385–399. [CrossRef]
72. Miller, I.M.; Warrick, J.A. Measuring sediment transport and bed disturbance with tracers on a mixed beach. *Mar. Geol.* **2012**, *299–302*, 1–17. [CrossRef]
73. Diplas, P.; Celik, A.O.; Valyrakis, M.; Dancey, C.L. Some Thoughts on Measurements of Marginal Bedload Transport Rates Based on Experience from Laboratory Flume Experiments. *US Geol. Surv. Sci. Investig. Rep.* **2010**, *5091*, 130–142.